

1 **Uncertainty quantification of ocean parameterizations:**
2 **application to the K-Profile-Parameterization for**
3 **penetrative convection**

4 **A. N. Souza¹, G. L. Wagner¹, A. Ramadhan¹, B. Allen¹, V. Churavy¹, J.**
5 **Schloss¹, J. Campin¹, C. Hill¹, A. Edelman¹, J. Marshall¹, G. Flierl¹, R.**
6 **Ferrari¹**

7 ¹Massachusetts Institute of Technology, 77 Massachusetts Ave, Cambridge, MA 02139, United States

8 **Key Points:**

- 9 • A Bayesian methodology can be used to probe turbulence parameterizations and
10 better understand their biases and uncertainties.
11 • Parameterization parameter distributions, learned using high-resolution simula-
12 tions, can be used as prior distributions for climate studies.

Abstract

Parameterizations of unresolved turbulent processes in the ocean compromise the fidelity of large-scale ocean models used in climate change projections. In this work, we use a Bayesian approach for evaluating and developing turbulence parameterizations by comparing parameterized models with observations or high-fidelity numerical simulations. The method obtains optimal parameter values, correlations, sensitivities, and, more generally, likely distributions of uncertain parameters. We demonstrate the approach by estimating the uncertainty of parameters in the popular ‘K-Profile Parameterization’, using an ensemble of large eddy simulations of turbulent penetrative convection in the ocean surface boundary layer. We uncover structural deficiencies and discuss their cause. We conclude by discussing the applicability of the approach to Earth system models.

Plain Language Summary

Climate projections continue to be marred by significant uncertainties, which originate in the poor representation of physical processes that occur at scales too minuscule for climate models to accurately simulate them, like clouds in the atmosphere and turbulent swirls in the ocean. We propose developing more accurate representations of small ocean processes (parameterizations) by training them with high-resolution numerical simulations of small ocean patches. A Bayesian methodology is used to calibrate the parameterizations with the high-resolution numerical simulations, to assess their fidelity and to identify improvements. Most importantly, this approach provides estimates of the uncertainties in the parameterizations, which can then be used to quantify uncertainties of climate models. While the method is illustrated for a parameterization of ocean turbulence, it can be applied to any parameterization in climate models.

1 Introduction

The ocean components of Earth system models are complex systems that couple the resolved ocean circulation with a myriad of unresolved, parameterized and important physical processes. Parameterizations of unresolved physical processes often involve many uncertain parameters which are used to tune the model in an attempt to obtain a desired outcome (Hourdin et al., 2017). Moreover, each component, whether resolved or parameterized, interacts with all the others in nonlinear ways that lead to complex behavior which is sometimes difficult to understand and characterize.

Upper ocean turbulent mixing is a key parameterized process in ocean circulation models. The detailed fluid dynamics of upper ocean turbulent mixing are highly complex, involving surface boundary layer turbulence driven by buoyancy loss or winds, bottom boundary layer turbulence, lateral mixing due to baroclinic effects, and so forth. However, at least in principle, the governing fluid dynamical equations are known. The problem is that the computational resources required to resolve them and, at the same time, the global scale circulation, are not available and will not be for the foreseeable future (Schneider, Teixeira, et al., 2017).

A goal of this paper is to outline and illustrate a Bayesian framework to assess and improve parameterizations. We present a way forward which employs an ensemble of mixing process resolving simulations to train a chosen parameterization. The core idea is that the parameterization must represent the collective effect of sub-grid scale physics faithfully for all relevant external forcings and mean climate states. This contrasts approaches that attempt to diagnose parameters directly from high-resolution simulations or to estimate values that perform well only in a particular experiment. It should be noted, however, that by restricting ourselves to understanding parameterizations in the context of sub-grid scale physics, we may miss out on important interactions with the rest of the climate system, e.g., the interaction of resolved lateral fluxes from the global

ocean circulation with parameterized turbulent vertical mixing in the ocean. Nevertheless, studying one subgrid-scale process at a time is not an exercise in futility since it is a necessary first step to optimize a parameterization before considering the interactions with all other components of the full system.

We take a Bayesian perspective in our optimization of parameterizations. There are many ways in which a Bayesian framework can be used. Here we will explore one particular approach: characterizing the parameters of a parameterization via probability distributions. Thus, we will go beyond finding a point estimate for parameters. These probability distributions capture the notion of uncertainty and nonlinear correlations between parameters. Furthermore, they can then be used as prior distributions for parameter sensitivity studies in full climate models. This partially addresses a present deficiency in the current approach used to tune parameters in climate models. “Manual” tuning is done to obtain agreement between models and observations (Hourdin et al., 2017). Since parameters are often correlated, a parameter may be tuned to offset biases introduced by another parameter, resulting in parameterizations that no longer respect the subgrid-scale physics. The Bayesian framework automates parameter search in a way that ensures it respects the underlying physics of a parameter. The calibration of parameterization schemes in climate models has the potential to reduce biases as well as quantify the uncertainty of key climate variables, such as ocean heat content or climate sensitivity; however, innovation is required to make the Bayesian method practical and computationally feasible in the global model. One step towards this is to calculate prior distributions for parameters in a simplified setting, such as the local studies performed here, and then use computationally efficient methods for obtaining posterior distributions in the global climate model such as those proposed in (Schneider, Lan, et al., 2017; Albers et al., 2019; Cleary et al., 2020).

The focus here is to calculate prior distributions for parameters in ocean climate models. We do so by matching parameterizations to large eddy simulations, a philosophy similar in spirit to that which has been done in the atmospheric context for cloud parameterizations (Golaz et al., 2007). To make our discussion concrete we focus on the representation of convectively-driven turbulence in the upper ocean.

Our paper is organized as follows: In section 2 we describe the physical scenario in which we run our Large Eddy Simulations (LES) and parameterization. In section 3 we introduce Bayesian parameter estimation for the parameters in the K-Profile Parameterization (KPP) and perform the parameter estimation in the regime described by section 2. Finally, we end with a discussion in section 4.

2 Large eddy simulations and K-Profile Parameterization of penetrative convection

During the onset of winter at high latitudes, cooling at the ocean surface generates convective plumes that descend and mix the ocean surface boundary layer, see Marshall and Schott (1999) for a review. Near-surface mixing by convection generates a surface layer of uniform temperature and salinity called the ‘mixed layer’ which can reach depths of hundreds of meters.

At the base of the mixed layer, convective plumes penetrate further into a strongly-stratified region called the ‘entrainment layer’, where plume-driven turbulent mixing between the mixed layer and the ocean interior further cools the boundary layer. This process, in which the surface layer is cooled both at the surface and by turbulent mixing in the entrainment layer, is called penetrative convection. Penetrative convection is a crucial oceanic process for storing heat and carbon as well as setting the density structure of the deep ocean. Parameterizations of ocean surface boundary layer mixing must describe penetrative convection accurately. In this paper we evaluate the accuracy of the

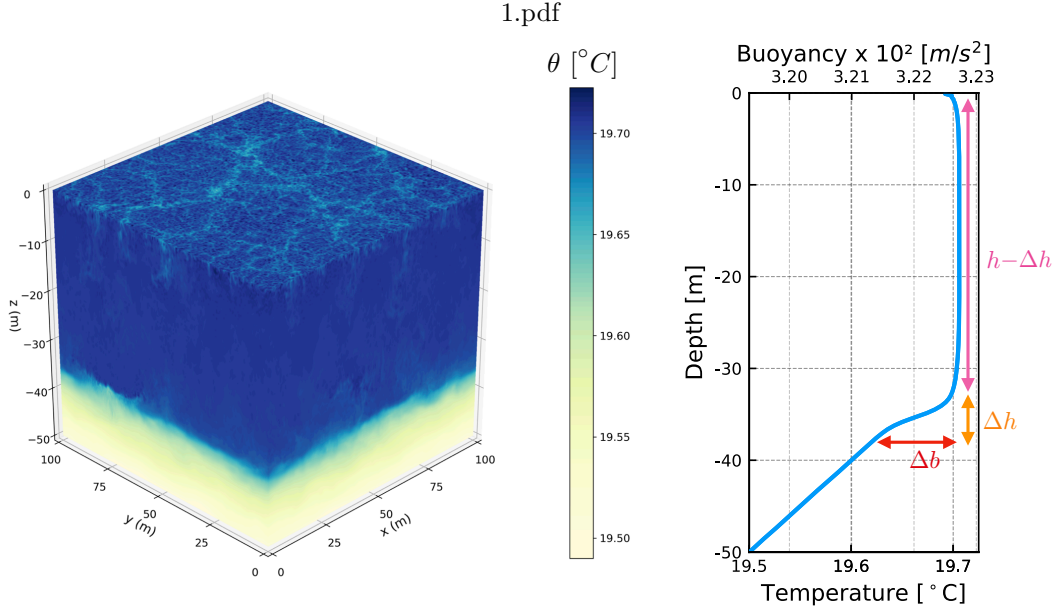


Figure 1. A 3D simulation of the LES model of the Boussinesq equations and its horizontal average at $t = 2$ days.

112 K-Profile Parameterization (Large et al., 1994) against large eddy simulations (LES) of
 113 idealized penetrative convection scenarios.

114 2.1 Idealized penetrative convection scenario

Our idealized scenarios impose a constant surface cooling $Q_h > 0$ to a resting, linearly stratified boundary layer with the initial state

$$\mathbf{u}|_{t=0} = 0 \text{ and } b|_{t=0} = N^2 z, \quad (1)$$

where $\mathbf{u} = (u, v, w)$ is the resolved velocity field simulated by LES, b is buoyancy, and N^2 is the initial vertical buoyancy gradient. The surface buoyancy flux Q_b is related to the imposed surface cooling Q_h , which has units W m^{-2} , via

$$Q_b = \frac{\alpha g}{\rho_{\text{ref}} c_p} Q_h, \quad (2)$$

115 where $\alpha = 2 \times 10^{-4} (\text{°C})^{-1}$ is the thermal expansion coefficient, $g = 9.81 \text{ m s}^{-2}$ is grav-
 116 itational acceleration, $\rho_{\text{ref}} = 1035 \text{ kg m}^{-3}$ is a reference density, and $c_p = 3993 \text{ J/(kg °C)}$
 117 is the specific heat capacity. Our software and formulation of the large eddy simulations
 118 is discussed in Appendix A.

Output of a large eddy simulation of turbulent penetrative convection in a domain $L_x = L_y = L_z = 100$ meters is in Figure 1. The left panel in Figure 1 visualizes the three-dimensional temperature field $\theta = \theta_0 + b/\alpha g$ associated with the buoyancy b , where $\theta_0 = 20 \text{ °C}$ is the surface temperature at $z = 0$. The right panel of Figure 1 shows the horizontally averaged buoyancy profile

$$\bar{b}(z, t) \equiv \frac{1}{L_x L_y} \int_0^{L_x} \int_0^{L_y} b(x, y, z, t) dx dy. \quad (3)$$

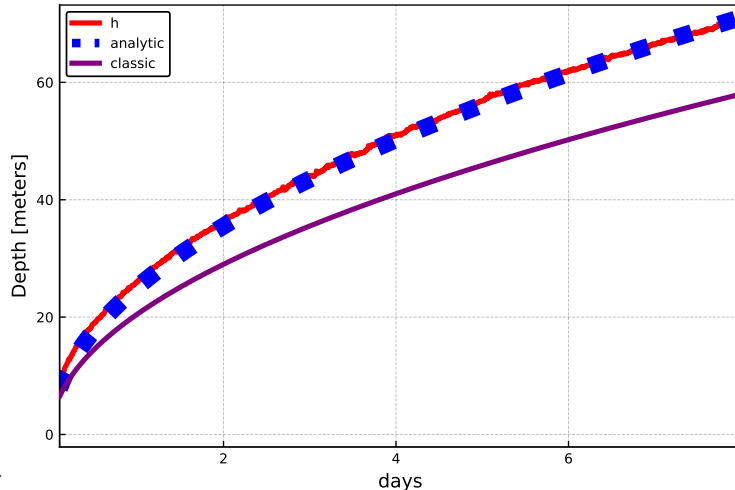


Figure 2. Mixed layer depth and its evolution in time after initial transients. The blue squares are the analytic scaling 4, the red line is an estimate of the boundary layer depth directly from the LES (described in the text), and the purple line is the classic scaling which ignores the entrainment layer 8.

119 The visualization reveals the two-part boundary layer produced by penetrative con-
 120 vection: close to the surface, cold and dense convective plumes organized by surface cool-
 121 ing sink and mix ambient fluid, producing a well-mixed layer that deepens in time. Be-
 122 low the mixed layer, the momentum carried by sinking convective plumes leads them to
 123 overshoot their level of neutral buoyancy (nominally, the depth of the mixed layer), ‘pen-
 124 etrating’ the stably stratified region below the surface mixed layer and generating the
 125 strongly stratified entrainment layer. The total depth of the boundary layer is h and in-
 126 cludes the mixed layer and the entrainment layer of thickness Δh . Turbulent fluxes are
 127 negligible below $z = -h$ for our purposes.

In figure 2 we show the evolution of $h(t)$ defined as the first depth from the bot-
 tom where the stratification is equal to a weighted average of the maximum stratifica-
 tion and the initial stratification¹. The dotted line confirms that the evolution after an
 initial transient is best fit by the formula,

$$h \simeq \sqrt{3.0 \frac{Q_b}{N^2} t}, \quad (4)$$

128 where N^2 is the initial stratification.

This result is easily explained by considering the horizontally averaged buoyancy
 equation,

$$\partial_t \bar{b} = -\partial_z (\overline{wb} + \overline{q^{(z)}}), \quad (5)$$

where \bar{b} is the horizontally averaged buoyancy, \overline{wb} is the horizontally averaged vertical
 advective flux and $\overline{q^{(z)}}$ is the horizontally averaged vertical diffusive flux. Integrating the

¹ The weights are 2/3 for the initial stratification N^2 and 1/3 for the maximum stratification N_m^2 so
 that h satisfies $\partial_z \bar{b}(-h) = 2N_b^2/3 + N_m^2/3$. This guarantees that h is a depth where the local stratification
 lies between the background stratification and the maximum stratification since it is defined as the *first*
 depth starting from the bottom that satisfies such a criteria.

equation in time between $t' = 0$ and some later time $t' = t$, and in the vertical between the surface, where $q^{(z)} = -Q_b$, and the base of the entrainment layer where all turbulent fluxes vanish, one finds,

$$\int_{-h}^0 [\bar{b}(z, t) dz - \bar{b}(z, 0)] dz = -Q_b t. \quad (6)$$

Substituting $\bar{b}(z, 0) = b_0 + N^2(z+h)$ and $\bar{b}(z, t) = b_0 + \Delta b$, which is an appropriate approximation of the profile shown in Fig. 1b except at very early times in the simulation, yields

$$\frac{1}{2} N^2 h^2 - h \Delta b = Q_b t. \quad (7)$$

The first term on the left of equation 7 describes boundary layer deepening due to buoyancy extraction at the surface, while the second term corresponds to the further cooling caused by turbulent mixing in the entrainment layer. Ignoring turbulent mixing in the entrainment layer yields the deepening rate

$$h = \sqrt{2.0 \frac{Q_b}{N^2} t}, \quad (8)$$

129 which differs by roughly 20% from the best fit expression 4 due to the effects of turbu-
 130 lent mixing in the entrainment layer. The scaling in equation 8 is the deepening rate as-
 131 sociated with a convective adjustment parameterization. The K-Profile Parameteriza-
 132 tion of penetrative convection, on the other hand, introduces a model for entrainment
 133 layer mixing in an attempt to describe equation 4.

134 2.2 The K-Profile Parameterization of penetrative convection

In penetrative convection in a horizontally-periodic domain, the K-Profile Parameterization models the evolution of the horizontally averaged temperature profile, $\theta(z, t)$, and the boundary layer depth with

$$\partial_t T = -\partial_z F(T, h; \mathbf{C}) \quad (9)$$

$$0 = \mathcal{D}(T, h; \mathbf{C}), \quad (10)$$

135 where T is the temperature profile produced by the K-Profile Parameterization, h is the
 136 boundary layer depth, $\mathbf{C} = \{C^S, C^N, C^D, C^H\}$ is a set of free parameters for represent-
 137 ing dimensionless proportionality constants following various scaling laws, $F(T, h; \mathbf{C})$ is
 138 a ‘temperature flux function’, and $\mathcal{D}(T, h; \mathbf{C})$ is a nonlinear-integral constraint to deter-
 139 mine the boundary layer depth. We emphasize that the goal of the parameterization is
 140 not limited to just getting the mixed layer depth correct or correctly predicting the jump
 141 in buoyancy. Rather, the goal is to obtain correct heat exchanges with the atmosphere,
 142 entrainment of nutrients for the biology, and flux rates of passive scalars. Thus, it is im-
 143 portant to faithfully capture the dynamics of the entire temperature profile.

The K-Profile Parameterization (KPP) represents F through the sum of a down-
 gradient flux and a non-local flux term (Large et al., 1994),

$$F = - \underbrace{C^D w_* h \frac{z}{h} \left(1 + \frac{z}{h}\right)^2}_{\equiv K} \partial_z T + \underbrace{C^N Q^\theta \frac{z}{h} \left(1 + \frac{z}{h}\right)^2}_{\equiv \Phi}, \quad (11)$$

144 for $-h \leq z \leq 0$ and 0 otherwise. Here $w_* = (Q_b h)^{1/3}$ is the convective turbulent ve-
 145 locity scale, h is the boundary layer depth, $\frac{z}{h} \left(1 + \frac{z}{h}\right)^2$ is the ‘K-Profile’ shape function—
 146 K is the namesake downgradient diffusivity of the K-Profile Parameterization—and Φ
 147 is a ‘non-local’ flux term that models convective boundary layer fluxes not described by
 148 downgradient diffusion.

In penetrative convection, the KPP model estimates the boundary layer depth h with an implicit nonlinear equation. To motivate the functional form of this criteria, first

see figure 1 for reference. The jump in buoyancy, Δb , is the difference between the buoyancy in the mixed layer and the base of the entrainment region. Equivalently we can write $\Delta b = N_e^2 \Delta h$, where N_e the stratification in the entrainment region. From plume theory, see Appendix B, we obtain $\Delta h \propto w_*/N_e$ so that

$$C^H = \frac{\Delta b}{w_* N_e} \quad (12)$$

for some universal proportionality constant C^H , which we call the ‘mixing depth’ parameter. KPP posits that the mixed layer depth h is the first such depth from the surface at which equation 12 holds. For numerical stability reasons equation 12 is generally formulated as

$$C^H = \frac{h \left[\frac{1}{C^{S_h}} \int_{-C^{S_h}}^0 B(z) dz - B(-h) \right]}{(hQ_b)^{1/3} h \sqrt{\max[0, \partial_z B(-h)]} + 10^{-11} \text{m}^2 \text{s}^{-2}}, \quad (13)$$

149 where $B = \alpha g T$. The numerator approximates the jump in buoyancy times the mixed
 150 layer depth, $h \Delta b$. The term, $\frac{1}{C^{S_h}} \int_{-C^{S_h}}^0 B(z) dz$, serves as an approximation to the buoy-
 151 ancancy in the mixed layer. The denominator evaluates the product $h w_* N_e$ with $w_* = (hQ_b)^{1/3}$
 152 and $N_e = \sqrt{\max[0, \partial_z B(-h)]}$ at a given depth, while adding a dimensional term 10^{-11}
 153 to prevent division by zero. In Appendix B we go in further detail about the rationale
 154 behind the implicit equation for the boundary layer depth, equation 13, for the case of
 155 penetrative convection.

156 The mixing depth parameter, C^H , is often referred to as the critical bulk Richard-
 157 son number in the KPP literature (Large et al., 1994), because in mechanically forced
 158 turbulence, the denominator is replaced by the mean shear squared times h . In pene-
 159 trative convection there is no mean shear and C^H is no longer related to a bulk Richard-
 160 son number.

The K-Profile Parameterization for penetrative convection has four free paramet-
 157 ers: the surface layer fraction C^S , the flux scalings C^N and C^D in equation 11, and the
 158 mixing depth parameter C^H in equation 13. Their default values, reported in (Large et
 159 al., 1994), are

$$(C^S, C^N, C^D, C^H) = (0.1, 6.33, 0.77, 0.95). \quad (14)$$

161 Our objective is to calibrate the free parameters $\mathbf{C} = (C^S, C^N, C^D, C^H)$ by compar-
 162 ing KPP temperature profiles $T(z, t; \mathbf{C})$ with the LES output $\bar{\theta}(z, t)$.

163 3 Model Calibration

We outline a Bayesian method for optimizing and estimating the uncertainty of the
 164 four free parameters through a comparison of solutions $T(z, t; \mathbf{C})$ to equation 9 to the
 165 output $\bar{\theta}(z, t)$ of our large eddy simulations. For this we define a loss function by

$$\mathcal{L}(\mathbf{C}) = \max_{t \in [t_1, t_2]} \left\{ \frac{1}{L_z} \int_{-L_z}^0 [T(z, t; \mathbf{C}) - \bar{\theta}(z, t)]^2 dz \right\}. \quad (15)$$

164 We choose the square error in space to reduce the sensitivity to vertical fluctuations in
 165 the temperature profile. In time we take the maximum value of the squared error to guar-
 166 antee that the temperature profile never deviates too far from the LES simulation at each
 167 instant.

168 Notably we do not use the boundary layer depth in the definition of the loss func-
 169 tion. Firstly, it should be stressed that getting the entire temperature profile correct is
 170 a more stringent requirement and would also imply a correct boundary (and mixed) layer
 171 depth. We prefer not to use a boundary layer depth directly because it leads to noisy

172 loss functions and depends too much on the precise definition used. In the literature, there
 173 are several different kinds of “depth” parameters based on, for example, the KPP def-
 174 inition as per equation 13, the location of the minimum buoyancy flux, the location of
 175 the maximum temperature gradient, or the first depth at which the temperature decreases
 176 by some ΔT of the surface value (Kara et al., 2000; Van Roekel et al., 2018). It is sim-
 177 pler (albeit more ambitious) to target the entire temperature profile. We prefer not to
 178 use the horizontally averaged temperature fluxes or gradients for practical reasons. Fluxes
 179 tend to be noisier than the horizontally averaged temperature profile and one would have
 180 to apply a smoothing filter. In summary, these other metrics introduce additional sources
 181 of systematic bias for little gain in the present circumstance.

182 A natural way to extend the definition of loss functions in order to take into ac-
 183 count parameter sensitivities is to define probability distributions for parameters. Sim-
 184 ilar to how the functional form of the loss function is critical to the estimation of opti-
 185 mal parameters, the functional form of a probability density is critical for estimating the
 186 uncertainties of a parameter. A probability distribution quantifies what we mean by “good”
 187 or “bad” parameter choices, (similar to a loss function), but in terms of uncertainties and
 188 likelihoods. It is often the case that one has a good feel for how to define meaningful loss
 189 functions, but less so for probability distributions. Here we report our choices, but in Ap-
 190 pendix C we provide guidance on criteria to be used when constructing as well as sam-
 191 pling from the probability distribution. It is worth keeping in mind that, just like loss
 192 functions, the true test is “after-the-fact”; we inspect results and confirm that they in-
 193 deed correspond to our intuition. Just like the definition of a loss function implicitly de-
 194 termines a choice of optimal parameters, a choice of probability distribution implicitly
 195 determines parameter sensitivities². Both are arbitrary, but that does not mean that loss
 196 functions or parameter sensitivities are meaningless.

We adopt the same definition as in (Schneider, Lan, et al., 2017) for the probabil-
 ity distribution:

$$\rho(\mathbf{C}) \propto \rho^0(\mathbf{C}) \exp\left(-\frac{\mathcal{L}(\mathbf{C})}{\mathcal{L}_0}\right) \quad (16)$$

197 where ρ^0 is the prior distribution of the parameter values, \mathcal{L} is a loss function, and $\mathcal{L}_0 >$
 198 0 is a *hyperparameter*³.

The loss function \mathcal{L} has dimensions and the parameter \mathcal{L}_0 makes the quantity in
 the exponent dimensionless. \mathcal{L}_0 could have been absorbed into the loss function, but it
 has a probabilistic interpretation that is worth emphasizing. We chose the parameter
 \mathcal{L}_0 as the minimum of the loss function $\mathcal{L}(\mathbf{C})$ —the minimum is found using a modified⁴
 simulated annealing procedure to compute the minimum of \mathcal{L} (Kirkpatrick et al., 1983).
 With this choice the likelihood of any other parameter choice, say \mathbf{C}^1 , is determined by
 the amount by which it increases the minimum of the loss function, i.e.,

$$\rho(\mathbf{C}^1)/\rho(\mathbf{C}^*) = \exp\left(\frac{\mathcal{L}^0 - \mathcal{L}(\mathbf{C}^1)}{\mathcal{L}^0}\right), \quad (17)$$

199 where \mathbf{C}^* denotes the optimal parameter choice with $\mathcal{L}^0 = \mathcal{L}(\mathbf{C}^*)$. For example, if the
 200 choice \mathbf{C}^1 increases the minimum of the loss function by a factor of two, i.e. $\mathcal{L}(\mathbf{C}^1) =$
 201 $2\mathcal{L}^0$, then it is $1/e$ less likely.

² Parameter sensitivities are inversely related to parameter uncertainties. A more sensitive parameter
 is one that produces larger changes to the loss function. In the context of this paper a more uncertain
 parameter is one that produces small changes to the loss function.

³ A hyperparameter is a parameter associated with the probability distribution as opposed to a param-
 eter in the parameterization.

⁴ The main difference is that we take the minimum “artificial temperature associated with the simu-
 lated annealing procedure” to be the best known minimum of the loss function \mathcal{L} rather than 0.

202 Once \mathcal{L}_0 is determined, we use the Random Walk Markov Chain Monte Carlo (RW-
 203 MCMC) algorithm (Metropolis et al., 1953), described further in C2, to sample the prob-
 204 ability distribution.

It is worth mentioning that equation 16 is the continuous analogue of Bayes for-
 mula

$$\mathbb{P}(\mathbf{C}|\text{data}) \propto \mathbb{P}(\mathbf{C})\mathbb{P}(\text{data}|\mathbf{C}) \quad (18)$$

205 where \mathbb{P} is a probability distribution. In our context we interpret the formula as follows:
 206 We update our prior belief of the distribution of parameters \mathbf{C} based on the data (in this
 207 case the LES experiment). $\mathbb{P}(\mathbf{C})$ is our prior probability for the parameters \mathbf{C} , while $\mathbb{P}(\text{data}|\mathbf{C})$
 208 is the probability that the parameter choices \mathbf{C} explain the data. Choosing to model pa-
 209 rameters as probability distributions has the consequence that the output of the param-
 210 eterization is also inherently probabilistic. In particular, the output of KPP will no longer
 211 be just a point estimate for temperature at each depth and each moment in time, but
 212 rather a probability distribution.

For all the uncertainty quantification that follows, we use resolution and timesteps
 typical of state of the art ocean models used for climate studies: a resolution of 100 m/16 =
 6.25 m and a timestep of ten minutes. The temporal window used to compute the loss
 function is from $t_1 = 0.25$ days to the final simulation day. We apply the Bayesian pa-
 rameter estimation procedure to KPP using data from one LES simulation in section 3.1
 and from multiple LES simulations using different initial stratifications in section 3.2.
 We use a uniform prior for the parameters in KPP over the following ranges:

$$0 \leq C^S \leq 1, \quad 0 \leq C^N \leq 8, \quad 0 \leq C^D \leq 6, \quad \text{and} \quad 0 \leq C^H \leq 5. \quad (19)$$

213 The surface layer fraction C^S , being a fraction, must stay between zero and one. The
 214 other parameter limits were chosen to correspond to “reasonable” ranges around the de-
 215 fault values, equation 14.

216 3.1 Calibration of KPP parameters against one LES simulation

217 In this section we apply the Bayesian calibration method to the LES simulation
 218 of penetrative convection described in section 2.1 and quantify uncertainties in param-
 219 eters of KPP, section 2.2. The horizontal averages from the LES simulations are com-
 220 pared with predictions from solutions of the KPP diffusion scheme. The boundary and
 221 initial conditions for KPP are taken to be the same as those for the LES simulation, i.e.,
 222 100 W/m² cooling at the top, $\partial_z T = 0.01^\circ\text{C m}^{-1}$ at the bottom, and an initial pro-
 223 file $T_p(z, 0) = 20^\circ\text{C} + 0.01^\circ\text{C m}^{-1}z$.

We use the RW-MCMC algorithm with 10⁶ iterations to sample the probability dis-
 tributions of the four KPP parameters (C^S, C^N, C^D, C^H). This lead to roughly 10⁴ sta-
 tistically independent samples as estimated using an autocorrelation length, see Sokal
 (1997). The RW-MCMC algorithm generates the entire four dimensional PDF, equation
 16, but visualizing this object is challenging. Instead we look at the marginal distribu-
 tions, e.g.,

$$\rho_M(C^H) \equiv \iiint \rho(\mathbf{C}) \, dC^S dC^D dC^N, \quad (20)$$

224 and similarly for the other parameters. (Constructing the marginal distributions only
 225 requires constructing histograms of the trajectories generated by the RW-MCMC algo-
 226 rithm.) Parameter correlations are washed away by focusing on marginal distributions.
 227 Nevertheless, marginal distributions give the range of parameter values that yield little
 228 change to the loss function and are shown in figure 3. The marginal distribution of the
 229 mixing depth parameter C^H is much more compact than that of the other three param-
 230 eters suggesting that it is the most sensitive parameter. The mixing depth parameter’s

231 importance stems from its control over both the buoyancy jump across the entrainment
 232 layer and the rate-of-deepening of the boundary layer. (Once again it may be useful to
 233 remember that C^H is often referred to the bulk Richardson number in the KPP liter-
 234 ature, even though it take a different meaning in convective simulations.) The param-
 235 eters C^K and C^N set the magnitude of the local and nonlocal fluxes and their specific
 236 value is not too important as long as they are large enough to maintain a well-mixed layer.
 237 The value of the regularization C^S is quite irrelevant.

238 The parameter distribution can be used to choose an optimal set of KPP param-
 239 eters. Of the many choices, we choose the most probably value of the four dimensional
 240 probability distribution, the mode, because they minimize the loss function as explained
 241 in Appendix C. (These values do not necessarily correspond to the individual modes of
 242 the marginal distributions. For example C^H is set to ≈ 2.0 rather than 1.5.) In figure
 243 4a we show the area averaged temperature profile after 8 days from the LES simulation
 244 (continuous line) and the temperature profiles obtained running the KPP parameteri-
 245 zation with default and optimal parameters (squares and dtots). The optimized temper-
 246 ature profiles are more similar to the LES simulation than the default value especially
 247 in the entrainment region. figure 4b confirms that the square root of the loss function,
 248 the error, grows much faster with the default parameters. The oscillations in the error
 249 are a consequence of the coarseness of the KPP model: only one grid point is being en-
 250 trained at any given moment.

251 The improvement in boundary layer depth through optimization of the parame-
 252 ters is about 10%, or 10 m over 8 days. As we discussed in section 2.1, the rate of deep-
 253 ening can be predicted analytically within 20% by simply integrating over time and depth
 254 the buoyancy budget and assuming that the boundary layer is well mixed everywhere,
 255 i.e. ignoring the development of enhanced stratification within an entrainment layer at
 256 the base of the mixed layer. KPP improves on this prediction by including a parame-
 257 terization for the entrainment layer. The default KPP parameters contribute a 10% im-
 258 provement on the no entrainment layer prediction, and the optimized parameters con-
 259 tribute another 10%. While these may seem like modest improvements, they can result
 260 into large biases in boundary layer depth when integrated over a few months of cooling
 261 in winter rather than just 8 days. We will return to this point in the next section when
 262 we discuss structural deficiencies in the KPP formulation.

263 The probability distributions of the parameters can be used to predict the prob-
 264 ability distributions of all variables, for example temperature at each depth and time,
 265 predicted by KPP. To do this, we subsample the 10^6 parameter values down to 10^4 and
 266 evolve KPP forward in time for each set of parameter choices. We construct histograms
 267 for the temperature field at the final time for each location in space individually. We then
 268 stack these histograms to create a visual representation of the model uncertainty. This
 269 uncertainty quantifies the sensitivity of the parameterization with respect to parame-
 270 ter perturbations as defined by the parameter distributions.

271 The histogram of temperature profiles at time $t = 8$ days as calculated by both
 272 our prior distribution (uniform distribution) and the posterior distribution (as obtained
 273 from the RW-MCMC algorithm) is visualized in figure 5. We see that there is a reduc-
 274 tion of the uncertainty in the temperature profile upon taking into account information
 275 gained from the LES simulation. The salient features of the posterior distribution tem-
 276 perature uncertainty are

- 277 1. 0-10 meter depth: There is some uncertainty associated with the vertical profile
- 278 of temperature close to the surface.
- 279 2. 20-60 meter depth: The mean profile of temperature in the mixed layer is very well
- 280 predicted by KPP.
- 281 3. 60-70 meter depth: The entrainment region contains the largest uncertainties.

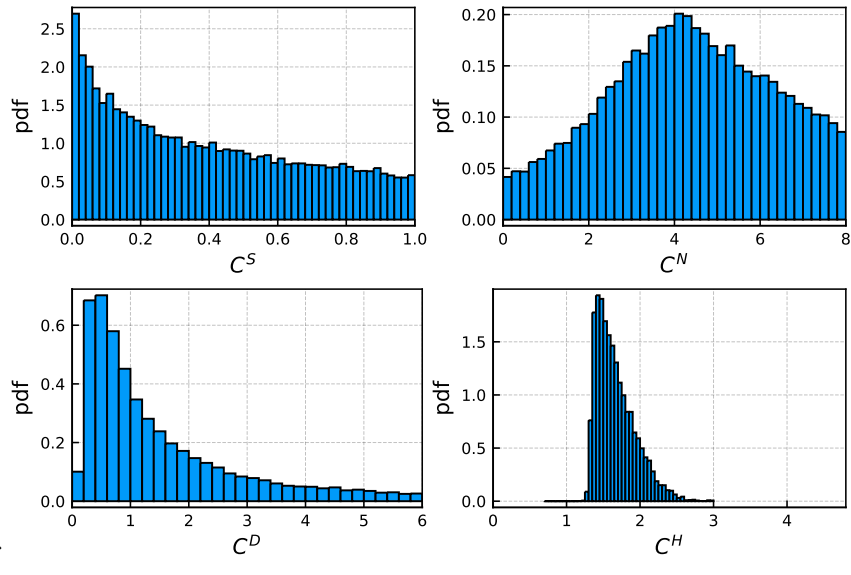


Figure 3. Parameter marginal posterior probability distributions. Marginal probability correspond to parameters parameters: C^S Surface Layer Fraction, C^N nonlocal diffusivity amplitude, C^D diffusivity amplitude, C^H mixing depth parameter. The probability distributions capture the notion of what parameter values are “good” and which ones are “bad”. For example, in the pdf for C^H we see that a value of 2.5 is probable but a value of 5 would be not be. This intuitively corresponds to saying that a value of 2.5 would be a “reasonable” choice whereas 5 would be “unreasonable”. The width of the C^S and C^N parameters suggest that KPP is quite insensitive to their values. A similar consequence holds for C^D , but there also seems to be a preference for values around one.

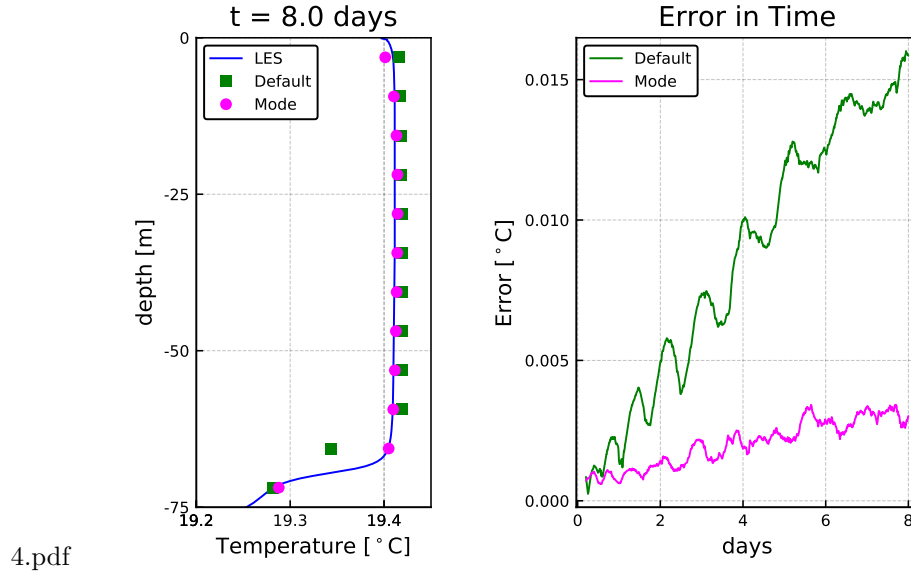


Figure 4. KPP and horizontally averaged LES temperature profiles for different point estimates of parameters at $t = 8$ days as well as the error in time. In the left plot, the squares correspond to default parameter choices, the circles correspond to the optimized parameterization (using the mode of the probability distribution), and the blue line to the horizontally averaged LES solution, all at time $t = 8$ days. On the right plot we show the instantaneous error at each moment in time. We see that the “optimal” parameter does indeed reduce the bias over the time period. The loss function is the largest square of the error over the time interval.

282 4. 70-100 meter depth: There is virtually no uncertainty. The unstratified region be-
 283 low the boundary layer does not change from its initial value.

284 Now that we have applied the Bayesian methodology to one LES simulation and
 285 explored its implications, we are ready to apply the method to multiple LES simulations
 286 covering different regimes in the following section. We focus on the optimization and un-
 287 certainty quantification of C^H for the remainder of the paper, since it is the most sen-
 288 sitive parameter. In the background, we are estimating *all* parameters.

289 3.2 Calibration of KPP parameters from multiple LES simulation

290 There are many possible directions that one could take at this point. We present
 291 an example of how we can use the methodology to explore bias in the KPP model. To
 292 this end we investigate what happens when we change the initial stratification in pen-
 293 etrative convection simulations. This is an informed decision motivated by recent work
 294 on mixed layer depth biases in the Southern Ocean (DuVivier et al., 2018; Large et al.,
 295 2019). In those studies, KPP failed to simulate deep mixed layer in winters when the sub-
 296 surface summer stratification was strong.

297 We perform 32 large eddy simulations and calculate parameter distributions for each
 298 case. We kept the surface cooling constant at 100 W/m^2 for all regimes, and only varied
 299 the initial stratification. The integration time was stopped when the boundary layer
 300 depth filled about 70% of the domain in each simulation. We used 128^3 grid points, \approx

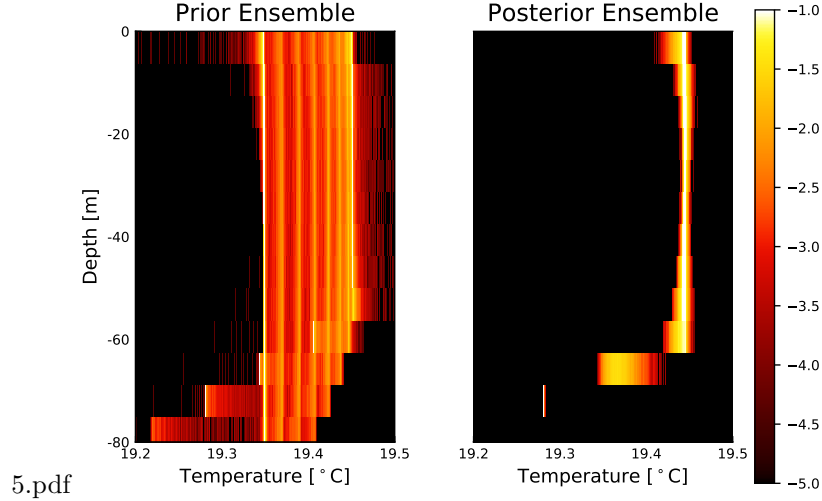


Figure 5. Uncertainty propagation of the temperature profile with respect to the prior and posterior probability distributions. The use of probability distributions for parameters has the consequence that the temperature field is no longer a point estimate, but rather a probability distribution at each moment in space and time. By sampling from the parameter probability distributions and evolving the parameterization forward in time, we obtain a succinct representation of what it means to “fiddle” with parameters. The legend on the right shows what the colors correspond to in terms of the base 10 logarithm of the probability distributions.

301 0.8 meter resolution in each direction⁵. Each one of the probability distributions used
 302 10^5 iterations of RW-MCMC, leading to effective sample size on the order of 10^3 .

303 The result, which is visualized in figure 6, shows that the parameter C^H depends
 304 on the background stratification, N^2 . The blue dots are the median values of the prob-
 305 ability distributions and the stars are the modes (minimum of the loss function). The
 306 error bars correspond to 90% probability intervals, meaning that 90% of parameter val-
 307 ues fall between the error bars. The default KPP value is plotted as a dashed line for
 308 reference.

309 The median values and optimal values increase monotonically with the initial strat-
 310 ification value. Given that the parameter is supposed to be dimensionless, this reveals
 311 a systematic bias. Furthermore, it exposes *where* the systematic bias comes from: the
 312 boundary layer depth criterion in equation 13. No single value of C^H can correctly re-
 313 produce the deepening of the boundary layer for all initial stratifications.

The failure of the depth criterion can be understood by going back to the buoy-
 ancancy budget in equation 7. Using the KPP estimate for the buoyancy jump across the
 entrainment layer,

$$\Delta b \equiv \frac{1}{C^S h} \int_{-C^S h}^0 B(z) dz - B(-h), \quad (21)$$

and introducing $N_h^2 \equiv \partial_z B(-h)$ for the stratification at the base of the entrainment
 layer to distinguish it from the interior stratification N^2 , we find that the boundary layer

⁵ Although the parameter estimates will vary upon using less resolution, the qualitative trends are expected to be robust.

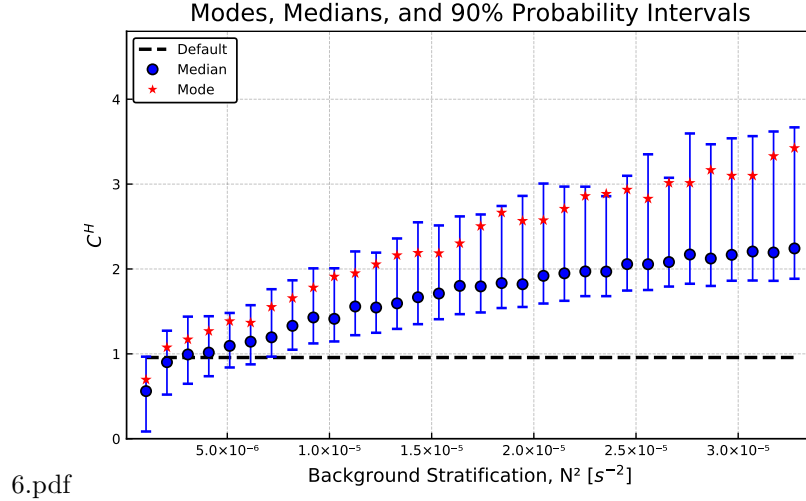


Figure 6. Mixing depth parameter optimized across various background stratification. The dots are the median values, the stars are the mode, and the error bars correspond to 90% probability intervals. The horizontal dashed line is the default value of the mixing depth parameter for reference. Here one can see that there mixing depth parameter when estimated across various regimes produces different results. This is a signature of a systematic bias in the parameterization.

depth criterion, equation 13, implies,

$$h\Delta b \simeq C^H h^{4/3} (Q_b)^{1/3} N_h. \quad (22)$$

Substituting this expression in the buoyancy budget, equation 7, one obtains an implicit equation for the evolution of the boundary layer depth h ,

$$\left(\frac{1}{2} N^2 - C^H (Q_b)^{1/3} h^{-2/3} N_h \right) h^2 \simeq Q_b t. \quad (23)$$

314 The LES simulation described in section 2.1, and many previous studies of penetrative
 315 convection, e.g. (Van Roekel et al., 2018; Deardorff et al., 1980), show that the bound-
 316 ary layer depth grows as \sqrt{t} . N_h would have to scale as $h^{2/3}$ for KPP to correctly pre-
 317 dict that deepening rate of the boundary layer, but this scaling is not observed in the
 318 LES simulations nor supported by theory.

3.3 Modification

319 From the multi-regime study of the previous section we found that there is no opti-
 mal KPP mixing depth parameter C^H that works for arbitrary initial stratification.
 This prompted us to look for an alternative formulation of the depth criterion which sat-
 isfies the well known empirical result that the boundary layer depth deepens at a rate,

$$h \simeq \sqrt{c \frac{Q_b}{N^2} t}, \quad (24)$$

where c is a dimensionless constant found to be close to 3.0 with the LES simulation in
 section 2.1. Furthermore, c was found to be close to 3.0 across all the numerical exper-
 iments from section 3.2. Substituting this expression in the buoyancy budget, equation
 7, we find that,

$$\frac{\Delta b}{h N^2} \simeq \left(\frac{1}{2} - \frac{1}{c} \right). \quad (25)$$

This expression can then be used as a new boundary layer depth criterion that replaces equation 13,

$$C^* = \frac{h \left(\frac{1}{C^* h} \int_{-C^* h}^0 B(z) dz - B(-h) \right)}{N^2 h^2 + 10^{-11} \text{m}^2 \text{s}^{-2}}, \quad (26)$$

where C^* replaces C^H as the dimensionless parameter whose value sets the boundary layer depth. Based on equation 25, we expect

$$C^* \simeq \left(\frac{1}{2} - \frac{1}{c} \right) \simeq \frac{1}{6}, \quad (27)$$

320 based on the LES result. The relation equation 26 is an implicit equation for h which
 321 guarantees that equation 24 holds. Once again, it may be useful to point out that C^*
 322 takes the place of what is generally referred to as the bulk Richardson number in the KPP
 323 literature, but that nomenclature is inappropriate for the case of penetrative convection
 324 where C^* parameterizes the effect of convective entrainment rather than shear mixing
 325 at the base of the mixed layer.

326 We now repeat the model calibration in section 3.2 with this new boundary layer
 327 depth criterion to test whether there is an optimal value of C^* that is independent of
 328 initial stratification. We estimate all KPP parameters and show the new mixing depth
 329 parameter for simulations with different initial stratifications in figure 7. There is no ob-
 330 vious trend in the optimal values of C^* and the error bars overlap for all cases. This val-
 331 idates the new criterion in that parameters estimated in different regimes are now con-
 332 sistent with one another. The uncertainties in C^* translate into an uncertainty in bound-
 333 ary layer depth prediction. In particular, values between $0.05 \leq C^* \leq 0.2$ imply a bound-
 334 ary layer depth growth in the range $\sqrt{2.22tQ_b/N^2} \leq h \leq \sqrt{3.33tQ_b/N^2}$.

335 Additionally one can check if the constants estimated with the methodology of sec-
 336 tion 3 are consistent with an *independent* measure directly from the diagnosed LES sim-
 337 ulation. In particular the LES simulations suggest that $C^* \simeq 1/6$ as per equation 27.
 338 From figure 7 we see that the optimal C^* is somewhat smaller than $1/6 = 0.167$ (the
 339 dashed black line). A reason for this discrepancy is the neglect of curvature in the buoy-
 340 ancancy budget, since we assumed a piece-wise linear buoyancy profile. Another one is the
 341 finite resolution in the model. A systematic source of error is how we diagnose the bound-
 342 ary layer depth: a different definition, such as the depth of maximum stratification, would
 343 yield a different scaling law (but still proportional to \sqrt{t}). At any rate the Bayesian pa-
 344 rameter estimation bypasses these ambiguities / inconsistencies by direct comparison with
 345 the LES data.

346 We do not explore other modifications to the boundary layer depth criterion as this
 347 would greatly expand the scope of this article. The criterion described in this section as-
 348 sumes a constant initial stratification and a constant surface heat loss, which leads to
 349 the \sqrt{t} growth of the boundary layer depth. It would be interesting to extend the cri-
 350 terion to arbitrary initial stratification, variable surface heat fluxes, not to mention the
 351 interaction with wind-driven mixing. The goal here was not to derive a new parameter-
 352 ization, but rather to introduce a methodology for obtaining meaningful parameteriza-
 353 tions for climate models.

354 4 Discussion

355 In this work we have used a Bayesian methodology for estimating parameters in
 356 parameterizations of subgrid-scale physics as a first step towards parameter sensitivity
 357 studies for Earth Systems Models. We have calculated parameter probability distribu-
 358 tions for parameters in the K-Profile Parameterization (KPP) by comparing with very
 359 high resolution simulations of ocean convection.

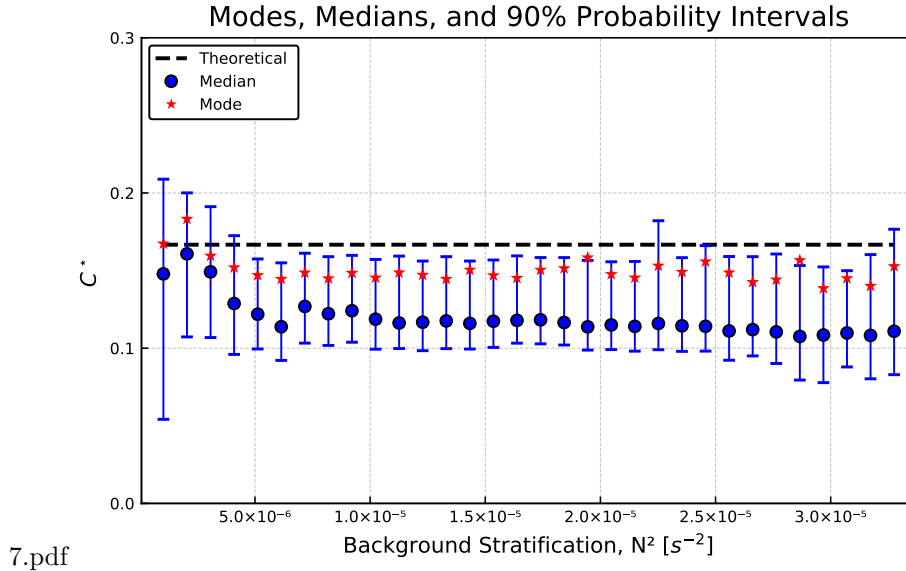


Figure 7. The modified mixing depth parameter optimized across various background stratification. The dots are the median values, the stars are the mode, and the error bars correspond to 90% probability intervals. The dashed line corresponds to $1/6$, the theoretical expectation based on equation 27. This is similar to figure 6, but using the modification from section 3.3. Here one can see that there mixing depth parameter when estimated across various regimes produces similar results. This is a desirable feature in a parameterization.

360 This approach differs from current practice in ocean and climate modelling. Stan-
 361 dard practice is to estimate parameters from a high resolution simulation or field cam-
 362 paign, or to tune parameters to reduce biases in global simulations. For example, the nondi-
 363 mensional amplitude of the KPP eddy diffusivity would be estimated as the ratio of the
 364 flux to the gradient from a single or a few high resolution simulations, (Van Roekel et
 365 al., 2018), or field campaigns, (Large et al., 1994). This assumes at the outset that the
 366 parameters calibrated for one test case will apply to all other scenarios, something that
 367 should be demonstrated rather than assumed. The other common approach is to tune
 368 the parameters in global models to reduce biases in climate relevant variables like ocean
 369 heat uptake or sea surface temperature (Menemenlis et al., 2005; Sraj et al., 2016). This
 370 can result in parameter choices that are inconsistent with the subgrid-scale physics they
 371 are supposed to parameterize. Our approach, instead, relies on a suite of high resolu-
 372 tion simulations that span all the scenarios the parameterization is supposed to capture.
 373 Applying a Bayesian methodology, we then estimate the probability distributions for par-
 374 ameters which are consistent with the whole suite of high resolution simulations. It is
 375 worth pointing out that the methodology is computationally trivial once one has the LES
 376 solutions. The intellectual effort goes into identifying appropriate forms for the cost func-
 377 tions and probability distributions to guide the quantification of parameter values and
 378 their uncertainty.

379 We illustrated our approach to estimating KPP parameters for convection in a strat-
 380 ified ocean. We found that no unique set of parameters could capture the deepening of
 381 convection for different initial stratifications. We showed that a reformulation of the cri-
 382 terion to estimate the penetration depth of convection allowed us to find parameters that
 383 agreed well with the whole set of high resolution simulations. This shows the Bayesian
 384 approach is not only useful to estimate the probability distributions of parameter val-

385 ues in a parameterization, but it can also be used to identify and eliminate potential bi-
 386 ases in parameterizations.

387 Ultimately, the hope is that parameter probability distributions estimated in lo-
 388 cal regimes will be useful for estimating uncertainties in global climate models; however,
 389 when coupling different components together, new parameters are introduced and non-
 390 linear interactions between parameters can arise. Thus additional optimization is required
 391 for the full system and this requires innovation, because the methodologies described in
 392 this paper are not computationally feasibly when applied to larger systems. A promis-
 393 ing approach for the global climate system is the Calibrate, Emulate, and Sample (CES)
 394 philosophy as outlined in (Cleary et al., 2020). In the CES approach, one uses a prior
 395 distribution for parameters (such as the ones calculated here for KPP) in a climate model
 396 in order to generate a preliminary ensemble of parameters. One then evolves this ensem-
 397 ble according to a loss function (appropriate to the global model) to generate a set of
 398 points that serve as a good “nodes” for interpolation of the loss function (or, alterna-
 399 tively, the “forward map”). A model, also called the emulator/surrogate model, is then
 400 chosen as an interpolator: this can be, for example, a Bayesian Neural Network or a Gaus-
 401 sian Process. Then one uses the interpolated function to calculate the probability of the
 402 posterior distribution using classic algorithms like the RW-MCMC method. In this way,
 403 one avoids rerunning the climate model and instead leverages as much information as
 404 possible from limited data. The surrogate model can then be used to update the prior
 405 distribution and improve predictions of the global model.

406 Stated differently we do not allow for arbitrary parameter perturbations when try-
 407 ing to match a climate model to data, parameter perturbations must take into account
 408 prior information. We propose obtaining this prior information by using highly resolved
 409 local simulations of turbulence. These experiments must be carefully designed and take
 410 into account suites of subgrid scale processes that one might expect to encounter in a
 411 global ocean model: vertical mixing, baroclinic effects, Langmuir turbulence, surface wave
 412 effects, bottom boundary layer turbulence, etc. If the global problem still exhibits sig-
 413 nificant biases after using all available prior information then this suggests that there
 414 is a fundamental deficiency in our understanding of how the different components of the
 415 climate system interact with one another. In this way one can start decoupling where
 416 biases in climate models come from. When the physics of local processes are well under-
 417 stood, then the additional uncertainties induced by coupling different regimes can be iso-
 418 lated and scrutinized. One no longer allows for biases to compensate for one another.

419 Appendix A Oceananigans.jl

Oceananigans.jl is open source software for ocean process studies written in the Ju-
 lia programming language (Bezanson et al., 2017; Ramadhan et al., 2020; Besard et al.,
 2019). For the large eddy simulations (LESs) reported in this paper, Oceananigans.jl is
 configured to solve the spatially-filtered, incompressible Boussinesq equations with a tem-
 perature tracer equations. Letting $\mathbf{u} = (u, v, w)$ be the three-dimensional, spatially-filtered
 velocity field, θ be the conservative temperature, p be the kinematic pressure, f be the
 Coriolis parameter, and $\boldsymbol{\tau}$ and \mathbf{q} be the stress tensor and temperature flux due to sub-
 filter turbulent diffusion, the equations of motion are A1–A3,

$$\partial_t \mathbf{u} + (\mathbf{u} \cdot \nabla) \mathbf{u} + f \hat{z} \times \mathbf{u} + \nabla p = b \hat{z} - \nabla \cdot \boldsymbol{\tau}, \quad (\text{A1})$$

$$\partial_t \theta + \mathbf{u} \cdot \nabla \theta = -\nabla \cdot \mathbf{q}, \quad (\text{A2})$$

$$\nabla \cdot \mathbf{u} = 0. \quad (\text{A3})$$

The buoyancy b appearing in A1 is related to conservative temperature by a linear equa-
 tion of state,

$$b = \alpha g (\theta_0 - \theta), \quad (\text{A4})$$

420 where $\theta_0 = 20^\circ \text{C}$ is a reference temperature, $\alpha = 2 \times 10^{-4} (\text{°C})^{-1}$ is the thermal ex-
 421 pansion coefficient, and $g = 9.81 \text{ m s}^{-1}$ is gravitational acceleration at the Earth’s sur-
 422 face.

423 A1 Subfilter stress and temperature flux

The subfilter stress and momentum fluxes are modeled with downgradient closures, such that

$$\tau_{ij} = -2\nu_e \Sigma_{ij} \quad \text{and} \quad \mathbf{q} = -\kappa_e \nabla \theta, \quad (\text{A5})$$

424 where $\Sigma_{ij} \equiv \frac{1}{2} (\partial_i u_j + \partial_j u_i)$ is the strain rate tensor, and ν_e and κ_e are the eddy vis-
 425 cosity and eddy diffusivity of conservative temperature. The eddy viscosity ν_e and eddy
 426 diffusivity κ_e in equation A5 are modeled with the anisotropic minimum dissipation (AMD)
 427 formalism introduced by (Rozema et al., 2015) and (Abkar et al., 2016), refined by (Verstappen,
 428 2018), and validated and described in detail for ocean-relevant scenarios by (Vreugdenhil
 429 & Taylor, 2018). AMD is simple to implement, accurate on anisotropic grids (Vreugdenhil
 430 & Taylor, 2018), and relatively insensitive to resolution (Abkar et al., 2016).

431 A2 Numerical methods

432 To solve equations A1–A3 with the subfilter model in equation A5 we use the soft-
 433 ware package ‘`Oceananigans.jl`’ written in the high-level Julia programming language
 434 to run on Graphics Processing Units, also called ‘GPUs’ (Bezanson et al., 2017; Besard
 435 et al., 2019; Besard et al., 2019). `Oceananigans.jl` uses a staggered C-grid finite vol-
 436 ume spatial discretization (Arakawa & Lamb, 1977) with centered second-order differ-
 437 ences to compute the advection and diffusion terms in equation A1 and equation A2, a
 438 pressure projection method to ensure the incompressibility of \mathbf{u} , a fast, Fourier-transform-
 439 based eigenfunction expansion of the discrete second-order Poisson operator to solve the
 440 discrete pressure Poisson equation on a regular grid (Schumann & Sweet, 1988), and second-
 441 order explicit Adams-Bashforth time-stepping. For more information about the staggered
 442 C-grid discretization and second-order Adams-Bashforth time-stepping, see section 3 in
 443 (Marshall et al., 1997) and references therein. The code and documentation are avail-
 444 able for perusal at <https://github.com/climate-machine/Oceananigans.jl>.

445 Appendix B Plume Model Derivation of the Mixing Layer Depth Cri- 446 teria

We begin by considering the vertical momentum equation for a parcel punching through the transition layer,

$$w' \frac{dw'}{dz} \simeq -(b' - \bar{b}) \quad (\text{B1})$$

where b' is the buoyancy of the parcel, assumed to be equal to the mixed layer value and \bar{b} is the area mean buoyancy profile in the transition layer. This equation holds if the mean buoyancy profile is in hydrostatic balance and the area occupied by sinking plumes is small compared to the total area (Deardorff et al., 1980). Integrating from $z = -h + \Delta h$, where $w' \equiv w_e$, to $z = -h$, where the turbulence and particle descent vanish and hence $w' = 0$, gives,

$$(w_e)^2 \simeq N_e^2 \Delta h^2, \quad (\text{B2})$$

assuming that the background stratification N_e^2 is constant in the entrainment layer. Introducing Δb as the difference between the buoyancy in the mixed layer and that at the base of the transition layer, we have, $\Delta \bar{b} = N_e^2 \Delta h$, and hence,

$$\Delta \bar{b} \propto w^* N_e, \quad (\text{B3})$$

where we assumed that $w_e \propto w^*(-h + \Delta h)$. The criterion for diagnosing the mixing layer depth follows from this relationship; h is defined as the first depth z below the ocean surface where,

$$\frac{\Delta b_p(z)}{w^*(z)N_e(z)} = C^H, \quad (\text{B4})$$

447 for some universal constant C^H .

448 Appendix C A Primer on Probability Distributions

449 In defining a probability distribution, there are a few desirable features that enable us to make a direct connection to a loss function, \mathcal{L} :

- 451 1. In the limit of no uncertainty, a probability distribution should collapse to a delta function centered at optimal parameter values of the loss function.
- 452
- 453 2. The uncertainty of a parameter value should be determined in terms of its effect on the loss function.
- 454

There are many probability distributions that satisfy the above criteria, but we choose

$$\rho(\mathbf{C}) \propto \rho^0(\mathbf{C}) \exp(-\mathcal{L}(\mathbf{C})/\mathcal{L}_0), \quad (\text{C1})$$

455 where ρ^0 is a uniform prior distribution, \mathcal{L} is a loss function, and \mathcal{L}_0 is a hyperparameter. In the following subsections we hope to elucidate why we made our particular choices. In C1 we describe why we chose \mathcal{L}_0 as we did. In C2 we go into detail on how to sample the probability distribution via the RW-MCMC algorithm as well as intuition for what it is doing.

460 C1 Explanation for our choice of \mathcal{L}_0

461 We now describe what the parameter \mathcal{L}_0 means in more detail. The limit $\mathcal{L}_0 \rightarrow 0$ corresponds to no uncertainty. In this limit, the probability distribution collapses to a delta function centered around the global optimal parameters of the loss function. An easy way to see this is to interpret the definition of the probability distribution as a Boltzmann-Gibbs distribution where the loss function corresponds to the energy of the system, and the constant \mathcal{L}_0 is analogous to the temperature of the system, kT where k is the Boltzmann constant, and T is the temperature. In the limit of zero temperature, the system collapses to the lowest energy state, in this case, the minimum of the loss function. The alternative limit $\mathcal{L}_0 \rightarrow \infty$ corresponds to an uncertainty that reduces to the prior distribution, ρ^0 . In this case, information gained from loss function evaluations are uninformative. In analogy with the Boltzmann-Gibbs distribution this corresponds to infinite temperature and every energy state becomes equally likely (hence uninformative).

The maximum of the probability distribution is the mode. This value is directly related to the minimum of the loss function \mathcal{L} if the prior distribution is uniform. Indeed, letting \mathbf{C}^* denote the (global) minimum of the loss function and \mathbf{C} denote any other value, we get

$$\mathcal{L}(\mathbf{C}^*) \leq \mathcal{L}(\mathbf{C}) \Rightarrow \exp(-\mathcal{L}(\mathbf{C})/\mathcal{L}_0) \leq \exp(-\mathcal{L}(\mathbf{C}^*)/\mathcal{L}_0) \Rightarrow \rho(\mathbf{C}) \leq \rho(\mathbf{C}^*). \quad (\text{C2})$$

473 Hence the minimum of the loss function is the most probable value of the probability distribution independent of \mathcal{L}_0 for a uniform prior distribution.

475 As mentioned in section 3, we choose the hyperparameter \mathcal{L}_0 to be the minimum of the loss function \mathcal{L} . Let us take a step back and explain *why* we used this definition. Whatever the choice of \mathcal{L}_0 , we would like the uncertainties of parameters to be independent of the units for which we use to evaluate the loss function. Furthermore, we would

479 like for it to become smaller when there is less model bias and greater when there is more
 480 model bias. In other words, there is more uncertainty when the parameterization does
 481 a poor job of matching the “truth”. This second criteria suggests that \mathcal{L}_0 should be
 482 a monotonic function of the global minimum of the loss function (the bias) $\mathcal{L}(\mathbf{C}^*)$ where
 483 \mathbf{C}^* denotes the optimal parameter values. The first criteria, coupled with the fact that
 484 a perfect model would output a value of 0 for the loss function, yields a number of choices.
 485 We use the simple form $\mathcal{L}_0 \propto \mathcal{L}(\mathbf{C}^*)$, as it is consistent with the previous sentence. Stated
 486 differently, we take \mathcal{L}_0 to be proportional to model bias. It is perhaps more correct to
 487 think of \mathcal{L}_0 as corresponding to *differences* in the loss function. Here we are using the
 488 difference between the “best” parameter choice and a (perhaps) non-existent parameter
 489 choice that would correspond to a perfect model whose loss function value is zero.

490 In the case that we have a *perfect* model and *perfect* data this would correspond
 491 to no uncertainty in the parameters and we would go back to having a point estimate
 492 for parameter values. Our choice here naturally assumes that both our data and our loss
 493 function are “perfect”. If we have an idea of how imperfect our data or loss function may
 494 be, then this additional uncertainty should be taken into account in the choice of \mathcal{L}_0 , or
 495 more generally, in the functional form of the probability distribution. We do not con-
 496 sider this additional source of uncertainty here.

497 The choice that we have made for this parameter may be thought of as how far we
 498 are willing to deviate from optimal values while still producing small changes in the loss
 499 function. In other words it is an *e*-folding length defined by the minimum of the loss func-
 500 tion. In this sense, we do not prescribe the uncertainty of a parameter a priori, but in-
 501 stead, implicitly determine it from a choice of how far from optimal parameters that we
 502 are willing to deviate. One could spend a lifetime arguing about the finer details of a choice
 503 for this parameter, but ultimately this would detract from the real goal: to gain an un-
 504 derstanding of what happens when one perturbs parameters away from optimal values.
 505 Any choice of $\mathcal{L}_0 > 0$ would do this. The important part is to make clear how such a
 506 choice is made and why.

507 Admittedly, in practice it is seldom possible to find the true global optimum of \mathcal{L}
 508 and the best one could hope for is some approximate value that is the “best known” op-
 509 timal value $\tilde{\mathbf{C}}$ to get an approximate $\tilde{\mathcal{L}}_0 \equiv \mathcal{L}(\tilde{\mathbf{C}})$. Since $\mathcal{L}_0 = \mathcal{L}(\mathbf{C}^*) \leq \mathcal{L}(\tilde{\mathbf{C}}) = \tilde{\mathcal{L}}_0$,
 510 our uncertainty is a conservative estimate (recall that a smaller \mathcal{L}_0 corresponds to *less*
 511 uncertainty).

512 C2 Random Walk Markov Chain Monte Carlo

513 We use standard methods to sample values from the probability distribution. The
 514 algorithm that we describe here is the Random Walk Markov Chain Monte Carlo Method
 515 (RW-MCMC), first used in (Metropolis et al., 1953). This method is most appropriate
 516 for loss functions where gradient information is either unavailable or prohibitively ex-
 517 pensive to calculate. If it is possible to differentiate the loss function, then other meth-
 518 ods may be more efficient at sampling from the distribution, such as Hamiltonian Monte
 519 Carlo. This alternative method is especially relevant when one wants to estimate a large
 520 number of parameters; however, here we are estimating four parameters, and there is no
 521 need for additional complexity.

522 The Random Walk Markov Chain Monte Carlo (RW-MCMC) algorithm, as the name
 523 suggests, performs a random walk in parameter space \mathbf{C} . It stays in regions of high prob-
 524 ability more often, thereby allowing one to take the trajectories of the random walk and
 525 construct histograms that are directly related to the empirical distribution of underly-
 526 ing probability distribution function.

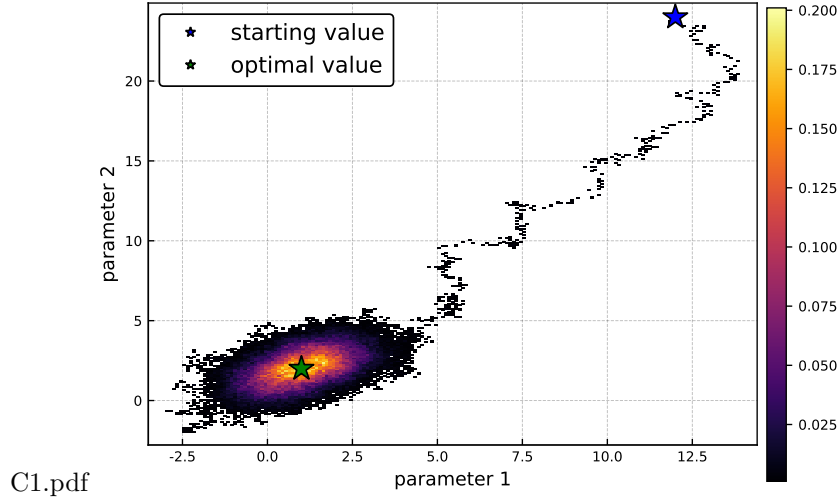


Figure C1. A histogram plot of RW-MCMC output for the target probability distribution equation C3 starting from a suboptimal value $\mathbf{C}^0 = [12.0 \ 24.0]^T$ and using 10^5 iterations. The white space signifies regions that the algorithm did not explore. The dark regions correspond to places that were rarely visited whereas the red and yellow regions correspond to places that were visited more often. The trail from the starting value to the optimal value illustrates how the random walk is biased towards regions of ever increasing probability.

We further illustrate what the algorithm does by considering the following toy loss function:

$$\mathcal{L}(\mathbf{C}) = \frac{1}{2}(\mathbf{C} - \boldsymbol{\mu})^T \Sigma^{-1}(\mathbf{C} - \boldsymbol{\mu}), \quad \boldsymbol{\mu} = \begin{bmatrix} 1 \\ 2 \end{bmatrix}, \quad \text{and} \quad \Sigma = \begin{bmatrix} 1 & 1/2 \\ 1/2 & 1 \end{bmatrix}, \quad (\text{C3})$$

527 with the choice $\mathcal{L}_0 = 1$ in the probability distribution. In figure C1 we show a typical
 528 output from an RW-MCMC algorithm for this probability distribution. Note that the
 529 optimal value of the loss function is $\boldsymbol{\mu} = [1 \ 2]^T$. Starting from a poor initial guess, here
 530 $\mathbf{C}^0 = [12.0 \ 24.0]^T$, the algorithm goes towards regions of higher probability (lower cost
 531 function) by randomly choosing which direction to go. Once a region of high probab-
 532 ility is found, in this case parameter values close to $\boldsymbol{\mu}$, the parameters hover around the
 533 minima of the loss function in a way that is consistent with the target probability dis-
 534 tribution.

535 We now go into detail on RW-MCMC algorithm. Ratios of the probability distribu-
 536 tion play a prominent role in the RW-MCMC algorithm; however, due to finite pre-
 537 cision arithmetic considerations it is actually better to work with the logarithms of the
 538 probability distribution. A convenient way to do this is to use the negative log-likelihood
 539 function as $\ell = -\ln \rho$. In our context, this function can be thought of as being essen-
 540 tially the same as the loss function 15, but shifted and scaled. Denote elements of a se-
 541 quence of parameter values by \mathbf{C}_i . The RW-MCMC algorithm is:

- 542 1. Choose initial parameter values \mathbf{C}_0 . One choice for this parameter is the best known
- 543 minimizer of the log-likelihood function using standard minimization techniques.
- 544 2. Calculate a “proposal parameter” $\tilde{\mathbf{C}}_1$. This will be described in more detail later.
- 545 3. Calculate $\Delta \ell = \ell(\mathbf{C}_0) - \ell(\tilde{\mathbf{C}}_1)$. This is a measure of how much more likely $\tilde{\mathbf{C}}_1$
- 546 is relative to \mathbf{C}_0 .

- 547 4. Draw a random uniform random variable from the interval $[0, 1]$, e.g, calculate $u =$
 548 $\mathcal{U}(0, 1)$. This is used to determine whether or not to accept \mathbf{C}_1 as a new param-
 549 eter.
- 550 5. If $\log(u) < \Delta\ell$ set $\mathbf{C}_1 = \tilde{\mathbf{C}}_1$. Otherwise set $\mathbf{C}_1 = \mathbf{C}_0$. This is the “accept / re-
 551 ject” step. Note that if $\Delta\ell > 0$, i.e. the proposed parameter produces a smaller
 552 output in the negative log-likelihood function, the proposal is always accepted.
- 553 6. Repeat steps 2-5 for \mathbf{C}_i , replacing $\mathbf{C}_0 \rightarrow \mathbf{C}_i$ and $\mathbf{C}_1 \rightarrow \mathbf{C}_{i+1}$, to generate a se-
 554 quence (or chain) of parameter values.

555 Interpreting the negative log-likelihood function as a potential function, the algorithm
 556 may be succinctly stated as “always go downhill, sometimes go uphill”. The sequence
 557 of parameter values generated by this algorithm can then be used to construct any statis-
 558 tics of the probability distribution 16, including empirical distributions, marginal distri-
 559 butions, and joint distributions. In the context of KPP this can also generate the un-
 560 certainty of a temperature at a given point in space and time as well as the uncertainty
 561 of the mixed layer depth at a given time.

This random walk is different from a random number generator in that successive samples are not independent of one another but are instead correlated. The random walk must be run for enough time to generate a sufficient number of statistically independent samples. The proposal step is crucial to ensure this feature. Thus, we will now describe how to choose a proposal in more detail. If there are no restrictions on the range of parameter values, then one can perturb each parameter by a Gaussian random variable with mean zero and covariance matrix Σ , i.e.

$$\tilde{\mathbf{C}}_{i+1} = \mathbf{C}_i + \mathcal{N}(0, \Sigma) \quad (\text{C4})$$

562 Interestingly, the algorithm is guaranteed to work *independent* of the choice of Σ as long
 563 as the covariance matrix Σ is nonzero and the same proposal is used throughout the ran-
 564 dom walk⁶; however, suitable choices of Σ can speed up convergence to the probability
 565 distribution. At the end of an RW-MCMC run one can diagnose the “number of inde-
 566 pendent samples” by using approximations of the correlation length, see Sokal (1997).
 567 If Σ is too small then the acceptance rate will be too large since each proposal param-
 568 eter is barely any different from the original parameter. Too large of a proposal often
 569 yields too low acceptance rates since it is typically easier to propose a parameter asso-
 570 ciated with a region of low probability than high probability (thereby making it likely
 571 that one is choosing a point that is “uphill” more often than “downhill”). One option
 572 is to take Σ to be a diagonal matrix whose diagonal elements are proportional to the square
 573 10% of the default parameter values, i.e., the standard deviation of the proposal of each
 574 was about 10% and that each parameter component proposal was independent. A com-
 575 mon option is to choose Σ according to the covariance matrix of the prior distribution.
 576 Yet, another option is to perform a preliminary random walk to estimate the covariance
 577 of the target distribution and then use this estimated covariance matrix in a new ran-
 578 dom walk. In general, there is no rule that will always speed up convergence, but we found
 579 that the last method to gave the best results.

580 If we would like to restrict the parameters to be in a finite range it is as simple as
 581 making the random walk take place in a periodic domain in parameter space. Another
 582 option is to redefine the loss function so that it outputs infinity if one plugs in a value
 583 outside a specified range. We opt for the former since it does not “waste” function eval-
 584 uations.

⁶ If one decides to change the proposal one needs to start the random walk over and cannot reuse data generated from another proposal.

Acknowledgments

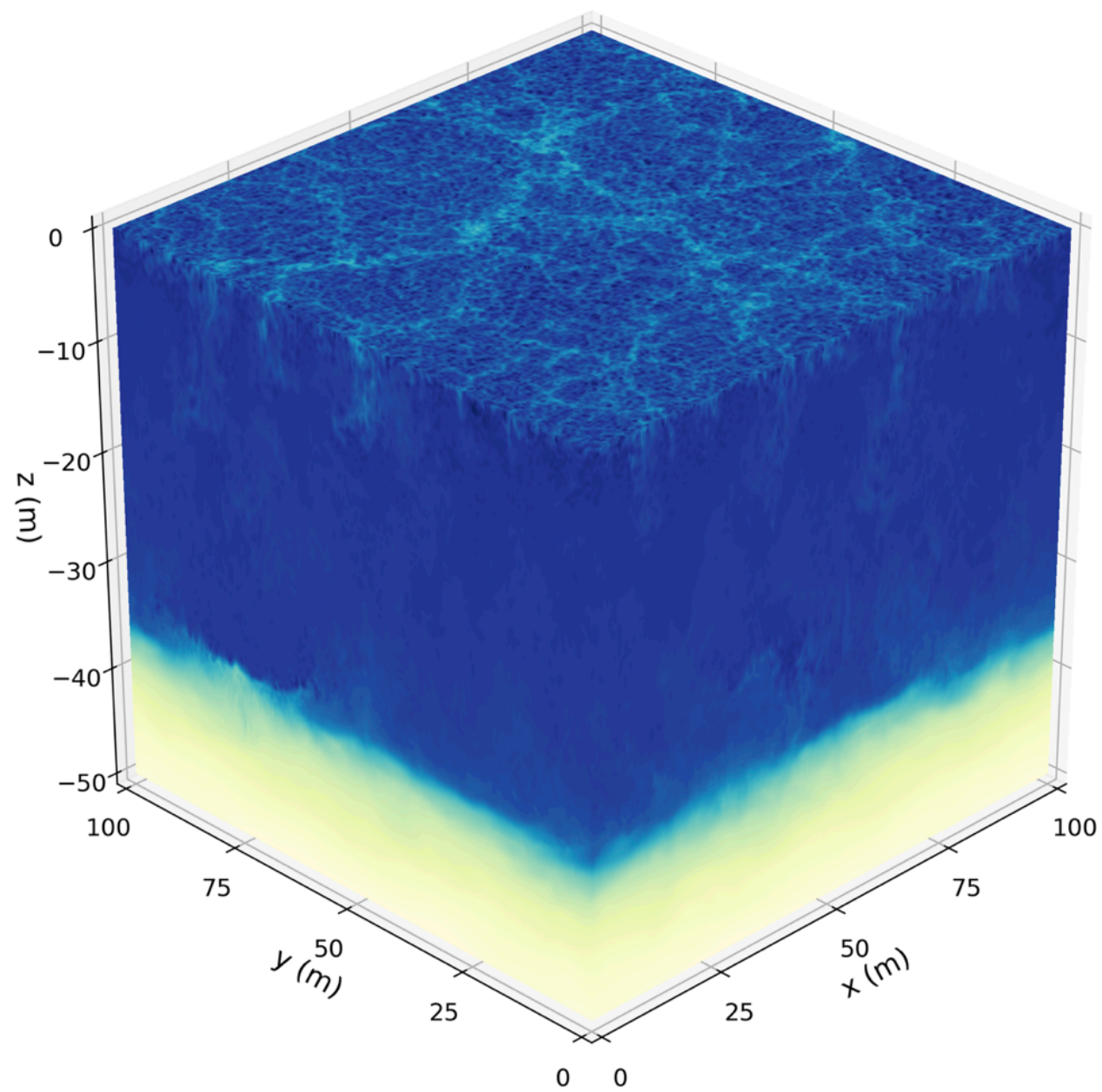
The authors would like to thank Carl Wunsch, Tapio Schneider, Andrew Stuart, and William Large for numerous illuminating discussions. Our work is supported by the generosity of Eric and Wendy Schmidt by recommendation of the Schmidt Futures program, and by the National Science Foundation under grant AGS-6939393.

References

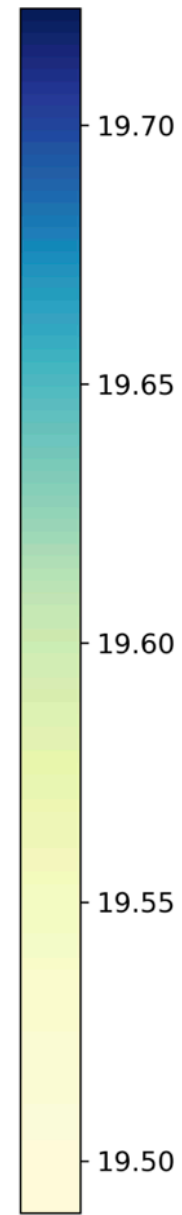
- Abkar, M., Bae, H. J., & Moin, P. (2016). Minimum-dissipation scalar transport model for large-eddy simulation of turbulent flows. *Physical Review Fluids*, *1*(4), 041701. doi: 10.1103/PhysRevFluids.1.041701
- Albers, D. J., Blancquart, P.-A., Levine, M. E., Seylabi, E. E., & Stuart, A. (2019). Ensemble kalman methods with constraints. *Inverse Problems*, *35*(9), 095007. doi: 10.1088/1361-6420/ab1c09
- Arakawa, A., & Lamb, V. R. (1977). Computational design of the basic dynamical processes of the ucla general circulation model. In J. Chang (Ed.), *General circulation models of the atmosphere* (Vol. 17, p. 173 - 265). Elsevier. doi: 10.1016/B978-0-12-460817-7.50009-4
- Besard, T., Churavy, V., Edelman, A., & Sutter, B. D. (2019). Rapid software prototyping for heterogeneous and distributed platforms. *Advances in Engineering Software*, *132*, 29 - 46. Retrieved from <http://www.sciencedirect.com/science/article/pii/S0965997818310123> doi: <https://doi.org/10.1016/j.advengsoft.2019.02.002>
- Besard, T., Foket, C., & De Sutter, B. (2019, April). Effective extensible programming: Unleashing julia on gpus. *IEEE Transactions on Parallel and Distributed Systems*, *30*(4), 827-841. doi: 10.1109/TPDS.2018.2872064
- Bezanson, J., Edelman, A., Karpinski, S., & Shah, V. B. (2017). Julia: A Fresh Approach to Numerical Computing. *SIAM Review*, *59*(1), 65–98. doi: 10/f9wkpj
- Cleary, E., Garbuno-Inigo, A., Lan, S., Schneider, T., & Stuart, A. M. (2020). Calibrate, emulate, sample. *arXiv:2001.03689 [stat.CO]*. Retrieved from <https://arxiv.org/abs/2001.03689>
- Deardorff, J. W., Willis, G. E., & Stockton, B. H. (1980). Laboratory studies of the entrainment zone of a convectively mixed layer. *Journal of Fluid Mechanics*, *100*(1), 4164. doi: 10.1017/S0022112080001000
- DuVivier, A. K., Large, W. G., & Small, R. J. (2018). Argo observations of the deep mixing band in the southern ocean: A salinity modeling challenge. *Journal of Geophysical Research: Oceans*, *123*(10), 7599-7617. doi: 10.1029/2018JC014275
- Golaz, J.-C., Larson, V. E., Hansen, J. A., Schanen, D. P., & Griffin, B. M. (2007). Elucidating model inadequacies in a cloud parameterization by use of an ensemble-based calibration framework. *Monthly Weather Review*, *135*(12), 4077-4096. doi: 10.1175/2007MWR2008.1
- Hourdin, F., Mauritsen, T., Gettelman, A., Golaz, J.-C., Balaji, V., Duan, Q., ... Williamson, D. (2017). The art and science of climate model tuning. *Bulletin of the American Meteorological Society*, *98*(3), 589-602. doi: 10.1175/BAMS-D-15-00135.1
- Kara, A. B., Rochford, P. A., & Hurlburt, H. E. (2000). An optimal definition for ocean mixed layer depth. *Journal of Geophysical Research: Oceans*, *105*(C7), 16803-16821. doi: 10.1029/2000JC900072
- Kirkpatrick, S., Gelatt, C. D., & Vecchi, M. P. (1983). Optimization by simulated annealing. *Science*, *220*(4598), 671–680. doi: 10.1126/science.220.4598.671
- Large, W. G., McWilliams, J. C., & Doney, S. C. (1994). Oceanic vertical mixing: A review and a model with a nonlocal boundary layer parameterization. *Reviews of Geophysics*, *32*(4), 363-403. doi: 10.1029/94RG01872

- 638 Large, W. G., Patton, E. G., DuVivier, A. K., Sullivan, P. P., & Romero, L. (2019).
639 Similarity theory in the surface layer of large-eddy simulations of the wind-,
640 wave-, and buoyancy-forced southern ocean. *Journal of Physical Oceanography*,
641 *49*(8), 2165-2187. doi: 10.1175/JPO-D-18-0066.1
- 642 Marshall, J., Adcroft, A., Hill, C., Perelman, L., & Heisey, C. (1997). A finite-
643 volume, incompressible navier stokes model for studies of the ocean on parallel
644 computers. *Journal of Geophysical Research: Oceans*, *102*(C3), 5753-5766. doi:
645 10.1029/96JC02775
- 646 Marshall, J., & Schott, F. (1999). Open-ocean convection: Observations, theory, and
647 models. *Reviews of Geophysics*, *37*(1), 1-64. doi: 10.1029/98RG02739
- 648 Menemenlis, D., Fukumori, I., & Lee, T. (2005, 05). Using green's functions to cali-
649 brate an ocean general circulation model. *Monthly Weather Review*, *133*, 1224-
650 1240. doi: 10.1175/MWR2912.1
- 651 Metropolis, N., Rosenbluth, A. W., Rosenbluth, M. N., Teller, A. H., & Teller, E.
652 (1953). Equation of state calculations by fast computing machines. *The*
653 *Journal of Chemical Physics*, *21*(6), 1087-1092. doi: 10.1063/1.1699114
- 654 Ramadhan, A., Wagner, G. L., Hill, C., Campin, J.-M., Churavy, V., Besard,
655 T., ... Ferrari, R. (2020). Oceananigans.jl: Fast and friendly geo-
656 physical fluid dynamics on GPUs. *The Journal of Open Source Soft-*
657 *ware*, *4*(44), 2018. Retrieved from [https://joss.theoj.org/papers/](https://joss.theoj.org/papers/aeb75d5b99d40ae6e0c8a3a4f09f3285)
658 [aeb75d5b99d40ae6e0c8a3a4f09f3285](https://joss.theoj.org/papers/aeb75d5b99d40ae6e0c8a3a4f09f3285) (Under review.)
- 659 Rozema, W., Bae, H. J., Moin, P., & Verstappen, R. (2015). Minimum-dissipation
660 models for large-eddy simulation. *Physics of Fluids*, *27*(8), 085107. doi: 10
661 .1063/1.4928700
- 662 Schneider, T., Lan, S., Stuart, A., & Teixeira, J. (2017). Earth system modeling
663 2.0: A blueprint for models that learn from observations and targeted high-
664 resolution simulations. *Geophysical Research Letters*, *44*(24), 12,396-12,417.
665 doi: 10.1002/2017GL076101
- 666 Schneider, T., Teixeira, J., Bretherton, C., Brient, F., Pressel, K., Schr, C., &
667 Siebesma, A. (2017, 01). Climate goals and computing the future of clouds.
668 *Nature Climate Change*, *7*, 3-5. doi: 10.1038/nclimate3190
- 669 Schumann, U., & Sweet, R. A. (1988). Fast fourier transforms for direct solution
670 of poisson's equation with staggered boundary conditions. *Journal of Compu-*
671 *tational Physics*, *75*(1), 123 - 137. doi: [https://doi.org/10.1016/0021-9991\(88\)](https://doi.org/10.1016/0021-9991(88)90102-7)
672 [90102-7](https://doi.org/10.1016/0021-9991(88)90102-7)
- 673 Sokal, A. (1997). Monte carlo methods in statistical mechanics: Foundations
674 and new algorithms. In C. DeWitt-Morette, P. Cartier, & A. Folacci (Eds.),
675 *Functional integration: Basics and applications* (pp. 131-192). Boston, MA:
676 Springer US. doi: 10.1007/978-1-4899-0319-8_6
- 677 Sraj, I., Zedler, S. E., Knio, O. M., Jackson, C. S., & Hoteit, I. (2016). Polyno-
678 mial chaosbased bayesian inference of k-profile parameterization in a general
679 circulation model of the tropical pacific. *Monthly Weather Review*, *144*(12),
680 4621-4640. Retrieved from <https://doi.org/10.1175/MWR-D-15-0394.1> doi:
681 10.1175/MWR-D-15-0394.1
- 682 Van Roekel, L., Adcroft, A. J., Danabasoglu, G., Griffies, S. M., Kauffman, B.,
683 Large, W., ... Schmidt, M. (2018). The kpp boundary layer scheme for the
684 ocean: Revisiting its formulation and benchmarking one-dimensional simula-
685 tions relative to les. *Journal of Advances in Modeling Earth Systems*, *10*(11),
686 2647-2685. doi: 10.1029/2018MS001336
- 687 Verstappen, R. (2018). How much eddy dissipation is needed to counter-
688 balance the nonlinear production of small, unresolved scales in a large-
689 eddy simulation of turbulence? *Computers & Fluids*, *176*, 276-284. doi:
690 10.1016/j.compfluid.2016.12.016
- 691 Vreugdenhil, C. A., & Taylor, J. R. (2018). Large-eddy simulations of stratified
692 plane Couette flow using the anisotropic minimum-dissipation model. *Physics*

Figure 1.



θ [$^{\circ}C$]



Buoyancy $\times 10^2$ [m/s^2]

3.20 3.21 3.22 3.23

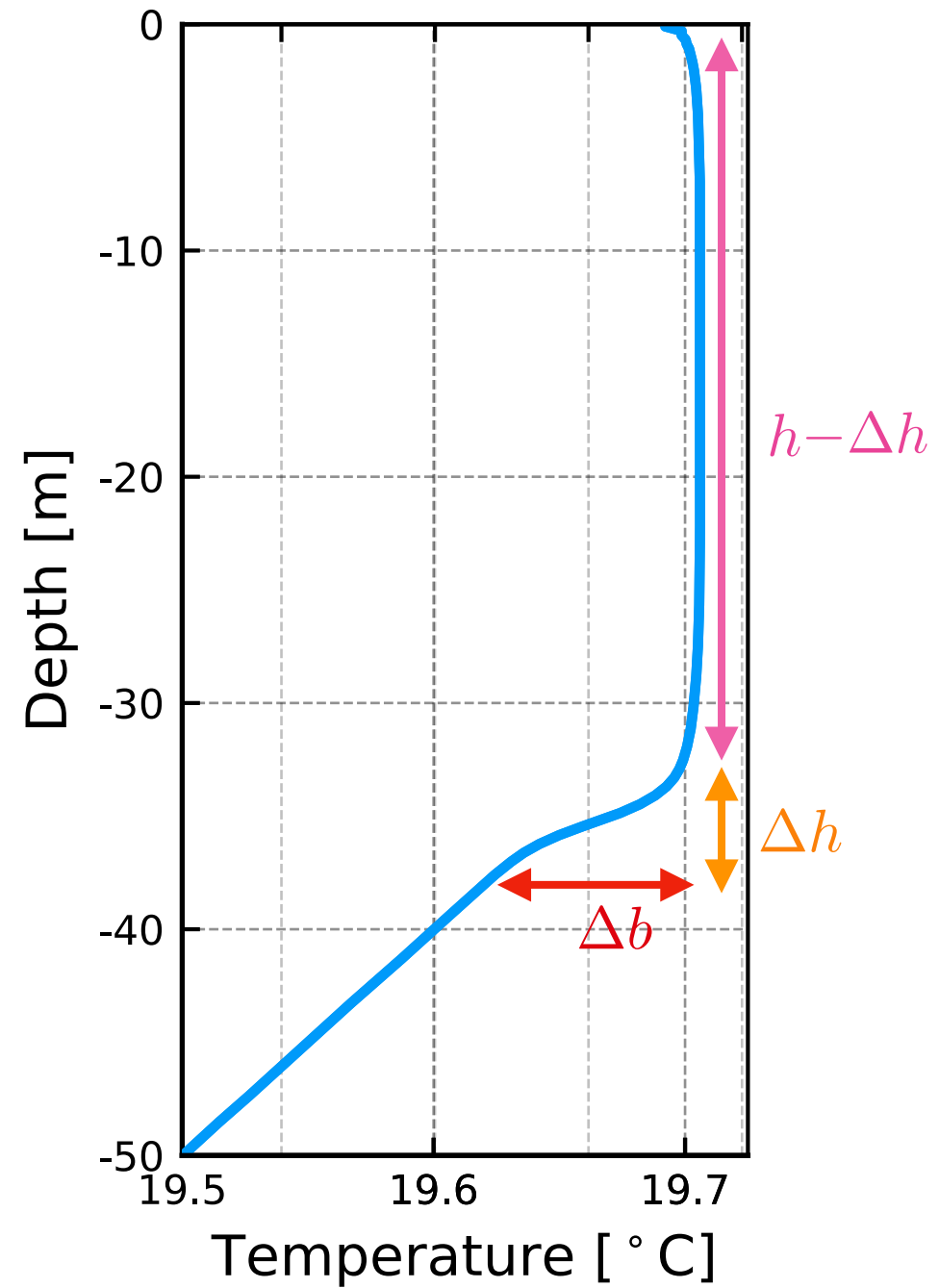


Figure 2.

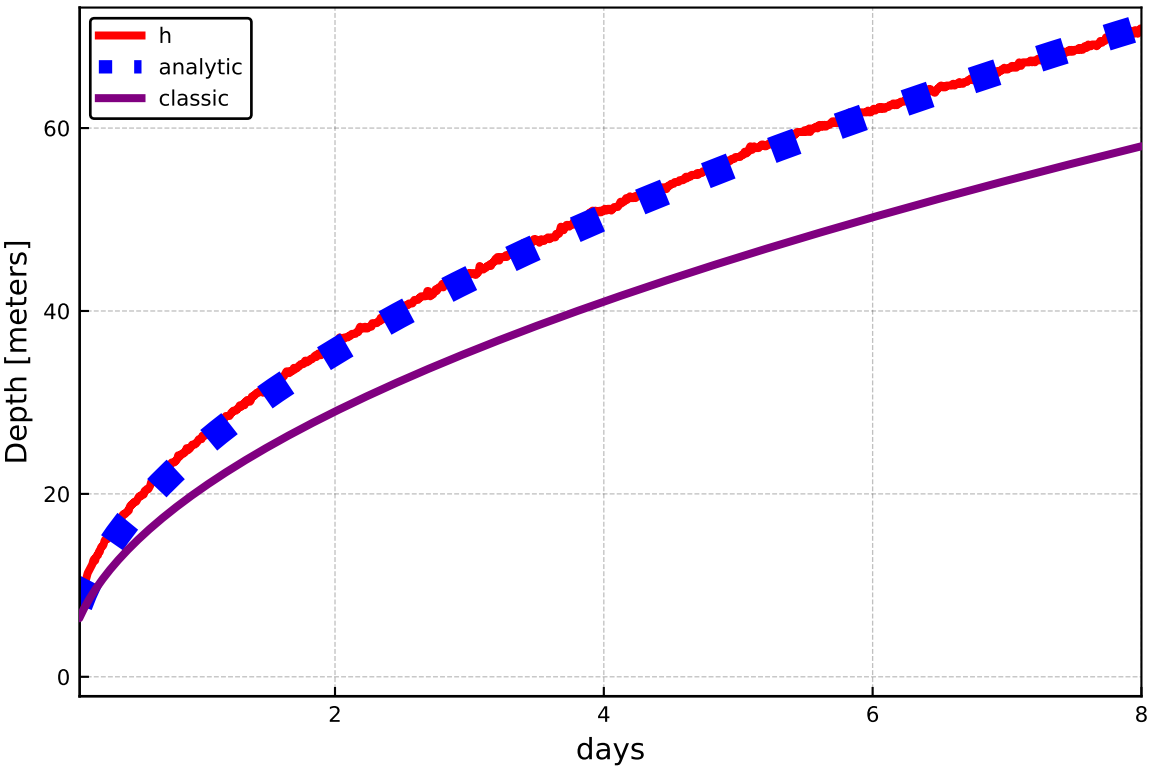


Figure 3.

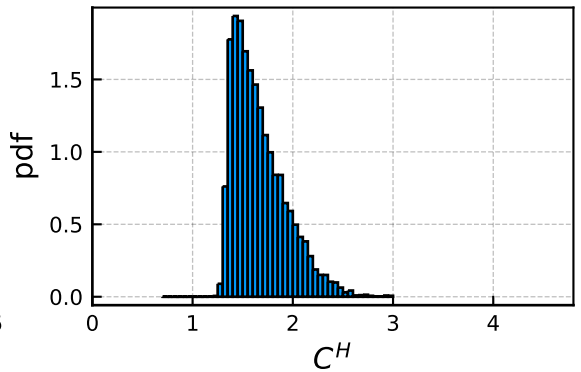
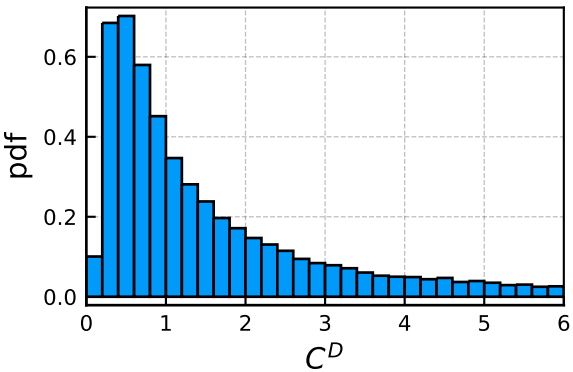
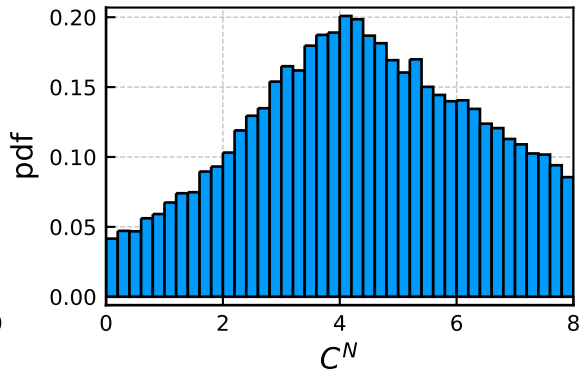
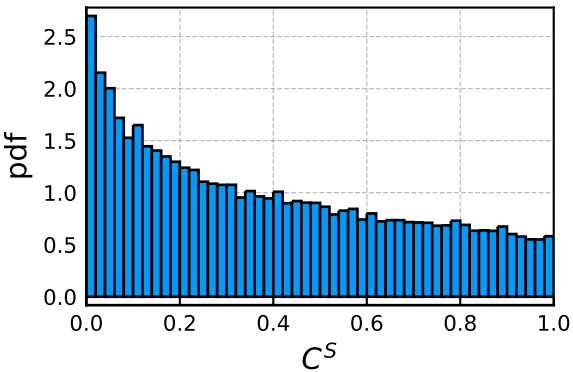
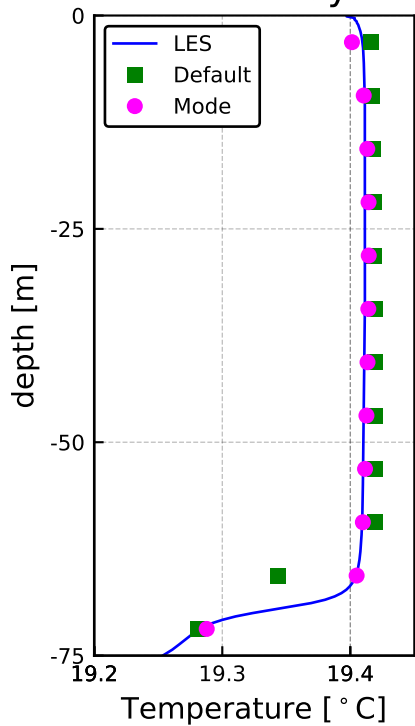


Figure 4.

t = 8.0 days



Error in Time

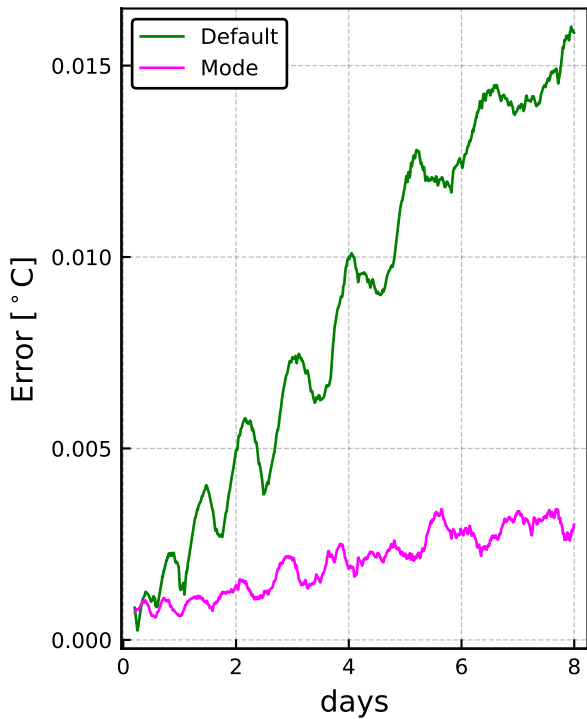
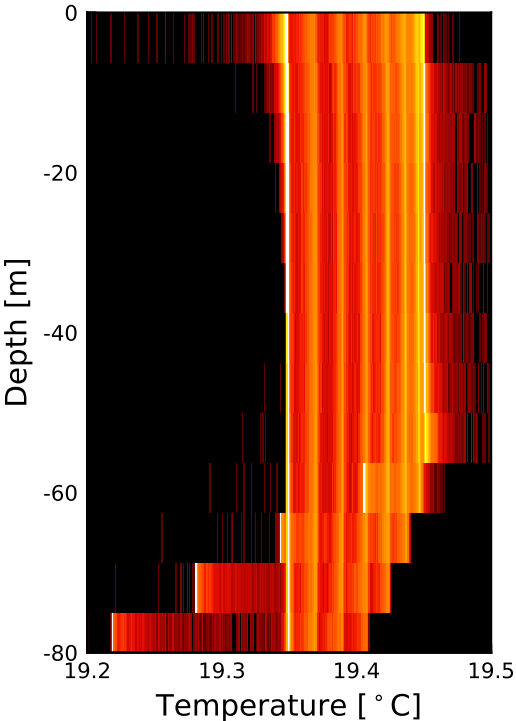


Figure 5.

Prior Ensemble



Posterior Ensemble

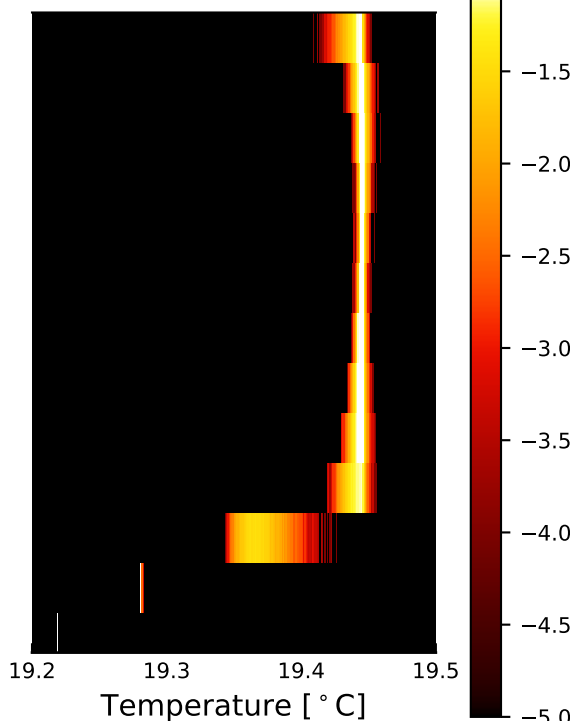


Figure 6.

Modes, Medians, and 90% Probability Intervals

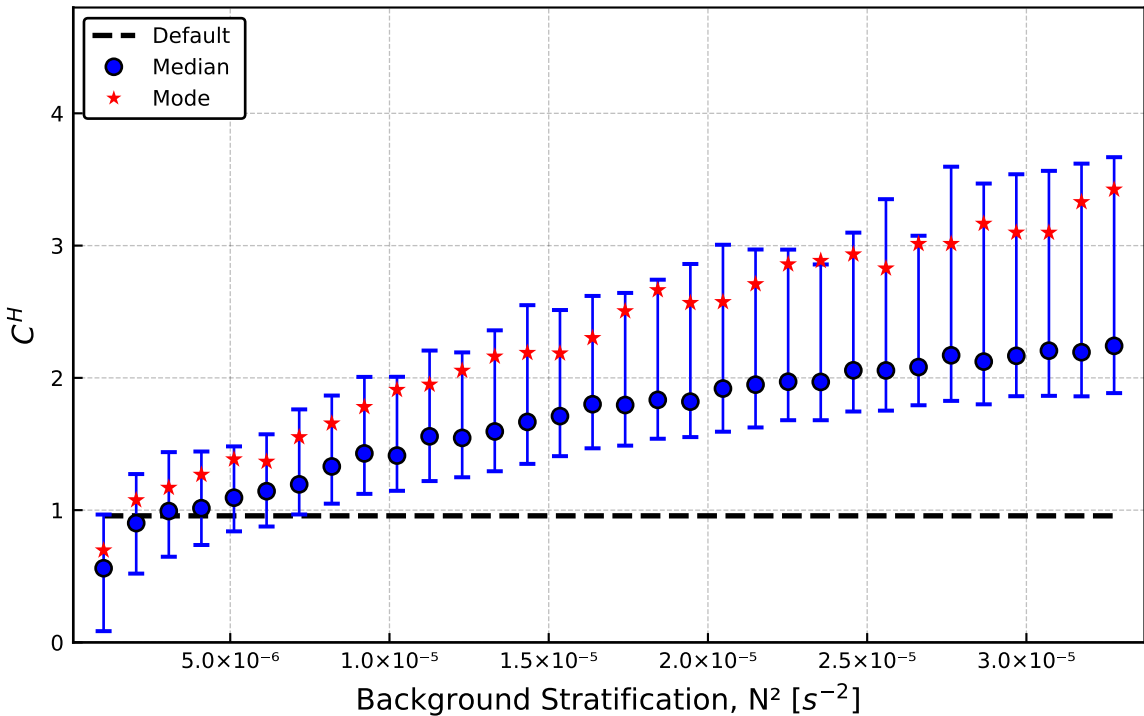


Figure 7.

Modes, Medians, and 90% Probability Intervals

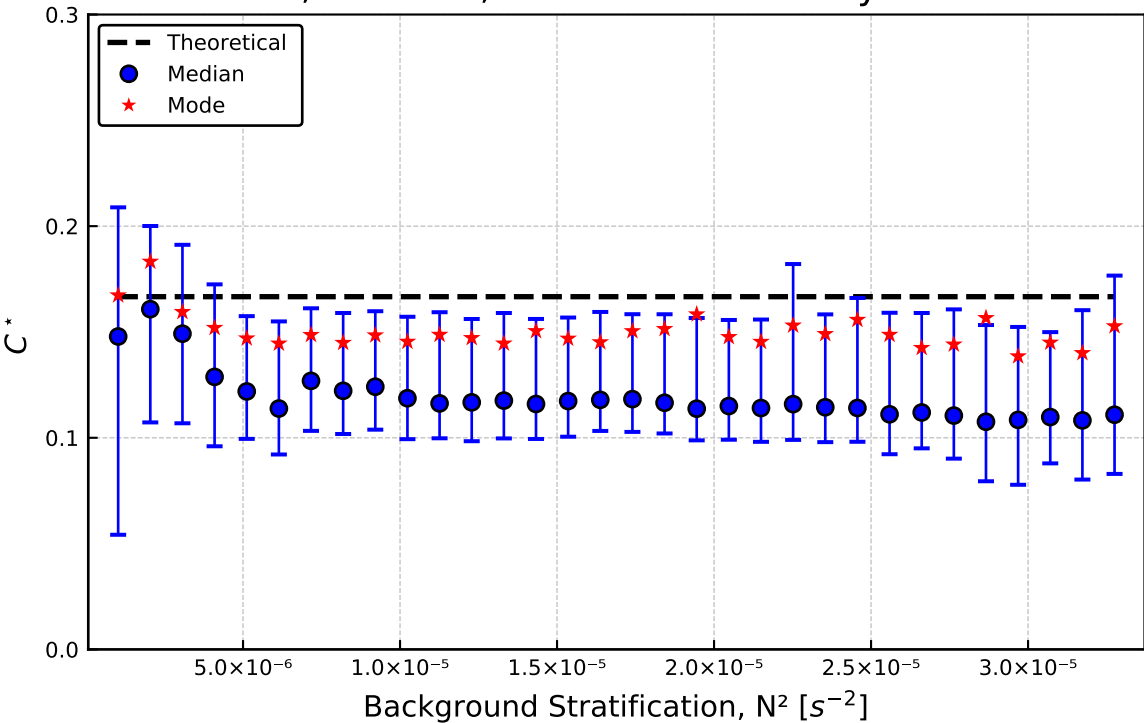


Figure C1.

